

1                   **The Quasi-Solid Box Method for Simulating Wind Around Obstacles in**  
2                   **the System for Atmospheric Modeling**

3  
4                   Marat F. Khairoutdinov<sup>1</sup>, Andrew M. Vogelmann<sup>2</sup>, and Katia Lamer<sup>2</sup>

5  
6                   <sup>1</sup> School of Marine and Atmospheric Sciences, Stony Brook University, Stony Brook, New York, USA

7                   <sup>2</sup> Brookhaven National Laboratory, Upton, New York, USA

8  
9  
10   Key points:

- 11       • A simple modification to the anelastic equations in the System for Atmospheric Modeling  
12       enables explicit resolution of the flow around buildings.
- 13       • The accuracy of the methodology is demonstrated using single-building wind tunnel data.

14  
15   **Abstract**

16  
17       A novel method to represent the flow around obstacles such as buildings is developed and  
18   incorporated into the System for Atmospheric Modeling (SAM). The Quasi-Solid Box Method (QSBM)  
19   introduces a simple modification to the anelastic equations that forces the flow to stagnate within the  
20   obstacle's boundaries. The performance of the modified SAM is evaluated using CEDVAL (Compilation  
21   of Experimental Data for Validation of Microscale Dispersion Models) wind tunnel measurements of the  
22   wind and tracer dispersion around a single rectangular building. All major flow features are well  
23   simulated, such as the arch vortex leeside of the building, height of the flow separation point in front of  
24   the building, "separation bubbles" over the rooftop and on building sides, and leeside return flow towards  
25   the building. The dispersion of the tracer released at the building base is also simulated quite reasonably.  
26   To demonstrate the ability of the method in more general cases when buildings boundaries do not conform  
27   to the grid-cell boundaries, we report results for successful simulation of a flow around a cubic building  
28   rotated by 45° relative to the flow, and around a building in the form of a cylinder of aspect ratio of one.  
29   The QSBM has virtually no additional computational cost and can be implemented in any anelastic model.

30  
Corresponding author: Marat Khairoutdinov, marat.khairoutdinov@stonybrook.edu

31 **Plain Language Summary**

32

33 A novel method to simulate the wind and turbulence around obstacles, such as buildings, has been  
34 developed for use in a computer model that was previously used only to study turbulence and clouds over  
35 flat Earth surface. The method, called the Quasi-Solid Box Method, forces the simulated flow to stop in  
36 the model grid-cells that are inside an obstacle. The accuracy of the method is tested using cases of a flow  
37 past an idealized single rectangular building, a cubic building rotated by 45°, and a building in the form  
38 of a cylinder. The simulations are compared with wind tunnel observations around a small model building  
39 and to results from other models. The modeled gas tracer dispersion around the building also agrees quite  
40 well observations. We also report results for successful simulation of a flow around a cubic building  
41 rotated by 45° relative to the flow, and around a building in the form of a cylinder of aspect ratio of one.  
42 The main appeal of the new method is its simplicity that requires very minor modifications to the model  
43 code. The improved model can be used for detailed studies of the impact of climate change on urban  
44 environments.

45

46

47 **1. Introduction**

48

49 Predicting how climate change will impact the Earth’s climate system is a longstanding goal that  
50 has motivated the development of an array of global climate models. Historically, climate models have  
51 been focused on predicting how climate change will impact natural environments. As 55% of the world’s  
52 population now lives in cities (Profiroiu et al., 2020), there has been growing interest in understanding  
53 how climate change will impact human stress as well and also how urban features themselves affect the  
54 stress level. Urban environments are visibly complex with their mix of land use and array of surface types.  
55 The high-level of heterogeneity and small scale of urban elements further motivates the general trend  
56 towards developing higher-resolution models.

57 The System for Atmospheric Modeling (SAM; Khairoutdinov & Randall, 2003) is a  
58 computationally efficient model that has been widely used within the community to study atmospheric  
59 processes. Its computational efficiency comes from the use of the anelastic approximation to the

60 momentum equations and is fully scalable to run as a cloud-resolving model at kilometer resolutions down  
61 to only a few meters as a large-eddy simulation model. This high degree of scalability presents an  
62 opportunity to simulate climate impacts on urban microclimates down to street-resolved resolutions. Such  
63 simulations, however, require an efficient way to represent heterogeneous urban landscapes and,  
64 particularly, how they affect wind flow and transport within streets and around buildings. Winds are  
65 chosen as a starting point as they act to ventilate heat, moisture and gas tracers and disperse of airborne  
66 contaminants. This paper provides a computationally efficient framework to make simulations building-  
67 aware in anelastic models such as SAM.

68         There are various methods for incorporating the impact of obstacles on wind flow in atmospheric  
69 models. The terrain-following coordinate transformation method (Gal-Chen & Somerville, 1975) has been  
70 used in many atmospheric models to incorporate the terrain. Unfortunately, its application may encounter  
71 some problems; for example, pressure gradient forces along a curved coordinate can lead to spurious flows  
72 at high model resolutions near steep terrain (e.g., Fortunato and Paptista, 1996). More importantly though,  
73 its application in SAM would require abandoning the use of the non-iterative bidirectional Fast Fourier  
74 Transform (FFT) solver for Poisson equation for pressure (which would include cross-derivatives),  
75 resulting in reduced computational efficiency and the need for development of an iterative elliptic equation  
76 solver.

77         There are other methods to modeling a flow past obstacles, such as buildings, in the computational  
78 fluid dynamics (CFD) community. One is to generate a curvilinear structured or unstructured grid that  
79 conforms to the obstacle's outer boundaries (e.g., Hanna, 2006; Blocken, 2018). However, in this case,  
80 modeling a different set of buildings would require generation of an entirely different grid. Local grid  
81 refinement would also be typically used to better resolve the flow near an obstacle's boundaries, especially  
82 when a building has a complex shape with many sharp edges. Arguably, this is the most comprehensive  
83 approach, but it may be quite complicated and computationally expensive, with complex grid-generation  
84 techniques that minimize the skewness of the resultant grids. Another popular method is the Immersed  
85 Boundary Method (IBM). In the IBM, the grid does not necessarily conform to the obstacle's outer  
86 boundaries and can be, for example, a regular Cartesian grid. For this method, an accurate algorithm is  
87 also needed to determine exactly where the buildings' surfaces lie relative to the specified grid. Then,  
88 carefully crafted forcing terms are added to the model momentum equations to force the velocity to be

89 tangential to the projected surface of an obstacle (e.g., Iaccarino and Verzicco, 2003; Mittal & Iaccarino,  
90 2005). The advantage of the IBM is that the obstacle’s actual boundaries are captured as opposed to being  
91 truncated by the grid cell boundaries. Also, for moving obstacles, the grid does not have to change; only  
92 the boundary’s current position should be recomputed. The IBM has been used in atmospheric models to  
93 simulate flow over terrain (Lundquist et al., 2010), blunt objects, and buildings in the atmospheric  
94 boundary layer (e.g., Lundquist et al., 2010; Kumar and Tiwari, 2021). However, implementing the IBM  
95 in SAM would not only require abandoning the FFT solver for the pressure equation, but it would also  
96 involve performing careful interpolation of the velocity flow at each time step, and possibly local grid  
97 refinement, to improve accuracy. As a result, it would lead to considerable code modifications and may  
98 generate complications arising from the requirement that, in the anelastic equations used in SAM, the  
99 predicted momentum field must be non-divergent at the end of each time step.

100 In one of the variants of the IBM, sometimes called the “body-force method”, the flow is not forced  
101 to be tangential to the projected building surface but, rather, fictitious nudging terms are used to force the  
102 velocity of the flow inside the obstacle to stagnate over a time horizon comparable to the model time step  
103 (Chen & Leach, 2007; Smolarkiewicz et al., 2007; Korycki et al. 2016; Muñoz-Esparza et al., 2020). An  
104 advantage of the body-force method is that it can also be used to represent porous obstacles such as trees.  
105 The nudging time scale is usually chosen to be inversely proportional to the wind velocity; as such, in  
106 high wind conditions the model time step may have to become very small for stability of the time  
107 integration scheme, which results in increase computational expense.

108 In this study, we propose and test a variant of the “body-force method”, which we call the Quasi-  
109 Solid Box Method (QSBM). In principle, the QSBM can be applied to any anelastic or Boussinesq model.  
110 The method allows one to halt the flow almost completely inside a chosen group of cells comprising an  
111 obstacle, and it does not require any explicit nudging terms. Also, the method does not impact the  
112 integration time step, which remains bounded by the usual Courant–Friedrichs–Lewy (CFL) stability  
113 constraint which is based on the resolved velocity already in SAM. The practical advantage of the QSBM

114 is that it is very simple and requires very minor code changes; further, the FFT solver for the pressure  
115 equation does not require any modifications, thus preserving SAM's computational efficiency.

116         The main drawback of the QSBM is that it requires approximation of an obstacle's shape by using  
117 only whole grid cells; this may create staircase-like boundaries for otherwise smooth boundaries that do  
118 not conform to the model grid, which may create additional noise and turbulence. However, this potential,  
119 additional turbulence is not considered to be of concern for the intended application of this method in  
120 SAM which is to simulate the flow and tracer transport around a city that is already immersed in a highly  
121 turbulent atmospheric boundary layer. This is fortunate as a rather coarse resolution is available to  
122 represent the many individual buildings within the city without incurring an enormous computational cost.  
123 We note that the real buildings, unlike many idealized models of buildings used in wind-tunnel  
124 experiments, have many irregular surface features—such as window cavities, balconies, architectural add-  
125 ons—that usually are not well represented by computer models anyway, but which can also produce  
126 turbulence. In addition, the turbulent flow in the boundary layer around real buildings itself is not very  
127 well resolved at small scales, even when large-eddy simulation (LES) is used. Within the context of the  
128 flow around the whole city, it is not clear how important all these details of the buildings (inherently  
129 unresolved by any LES) actually are to generating additional turbulence, which would require additional  
130 research in the future.

131         This paper is organized as follows. Details regarding the implementation of the QSBM in SAM  
132 are described in Section 2. A demonstration of the performance of the QSBM is provided in Section 3  
133 where we compare an LES of the flow past a single rectangular building against wind-tunnel  
134 measurements. In this case, the building orientation is such that its boundaries ideally conform to the  
135 Cartesian grid's cell boundaries. Therefore, in Section 4, we also demonstrate the generality of the method  
136 through results for two additional simulations of the flow around obstacles with the boundaries that do not  
137 conform to the grid cell boundaries. The first case is the flow around a cubic building rotated 45° to the  
138 direction of the flow, and the second case is the flow around a building in the form of a circular cylinder.  
139 A summary of the results is provided in Section 5.

140

## 141 **2. The Quasi-Solid Box Method (QSBM)**

142

143 Prognostic velocities in anelastic models, like SAM, cannot be simply set to zero at the boundaries  
144 of cells inside obstacle at the end of each time step because it would violate the non-divergence equation  
145 and lead to noise and numerical instability; thus, we design a method to produce a similar result. Like in  
146 the body-force method, the proposed QSBM adds a simple Newtonian damping nudging term to the  
147 momentum equations:

148

$$\frac{\partial \mathbf{u}}{\partial t} = \mathbf{A} - \nabla \pi - \frac{\mathbf{u}}{\tau} \quad (1)$$

149

150 where  $\mathbf{u}$  is the velocity vector,  $\nabla \pi$  is the pressure gradient,  $\tau$  denotes a damping time scale, and  $\mathbf{A}$  denotes  
151 all other terms like advection, diffusion, Coriolis force, etc. One can see that the damping term forces the  
152 wind to decelerate and eventually stop over some time. For the Arakawa-C grid, this damping term is  
153 activated for all the velocity components at the sides of each cell located inside an obstacle; otherwise, no  
154 damping is applied.

155 To reproduce the effect of wind stopping abruptly at the face of an obstacle,  $\tau$  in (1) should be  
156 infinitesimally small. However, since SAM uses the explicit third-order Adams-Bashforth (AB3) scheme  
157 for time integration, the minimum allowed value for  $\tau$  is approximately two time-steps for a non-  
158 oscillatory solution (Duran, 1991); otherwise, the computations would be unstable or oscillatory. As  
159 damping to near zero would take at least a time interval of  $3 \tau$ , or about six time-steps, it is obvious that  
160 such damping would be of no practical use—the flow would easily penetrate deep into the obstacle before  
161 stagnating; or, in the case of a relatively small obstacle, even go right through it. Therefore, a much smaller  
162 damping time scale is required.

163 One way to avoid numerical instabilities while introducing damping terms to the velocity  
 164 acceleration terms is to use an implicit scheme as follows. First, the provisional wind field  $\mathbf{u}^*$  is obtained  
 165 using only the  $\mathbf{A}$  terms:

$$166 \quad \mathbf{u}^* = \mathbf{u}^n + \Delta t^n (a\mathbf{A}^{n-1} + b\mathbf{A}^{n-1} + c\mathbf{A}^{n-2}) \quad (2)$$

167 where  $a$ ,  $b$ , and  $c$  are AB3 coefficients that depend on the current time step  $\Delta t^n$  and past time steps  
 168  $\Delta t^{n-1}$  and  $\Delta t^{n-2}$ . Next, the implicit correction to the provisional solution is made to include the  
 169 damping term:

$$170 \quad \mathbf{u}^{**} = \mathbf{u}^* - \mathbf{u}^{**} \frac{\Delta t^n}{\tau} \quad (3)$$

171 noting here that the implicit approximation (3) is computationally stable for any value of  $\tau$ . Equation (3)  
 172 can be rewritten as

$$173 \quad \mathbf{u}^{**} = \mathbf{u}^* \frac{1}{1 + \frac{\Delta t^n}{\tau}} \quad (4)$$

174 This form makes it easy to see that in the limiting case where flow comes to a complete stop at the obstacle  
 175 boundary for  $\tau = 0$ , or *instantaneous* relaxation, the factor  $\frac{1}{1 + \frac{\Delta t^n}{\tau}}$  becomes zero too. Given this, it is  
 176 sufficient to require that the *corrected provisional velocity*  $\mathbf{u}^{**}$  be zero at all sides of the cells inside an  
 177 *obstacle*, i.e.,

$$178 \quad \mathbf{u}^{**} = 0 \quad \text{at all sides of cells inside an obstacle} \quad (5)$$

179 and there is no need to specify a value for  $\tau$ . Note, however, that representing the flow through porous  
 180 obstacles such as bushes and trees would require setting some explicit value to the relaxation time-scale  
 181  $\tau$  in (4). The final solution can then be obtained by performing the pressure-correction step

$$182 \quad \mathbf{u}^{n+1} = \mathbf{u}^{**} - \Delta t^n (a\nabla\pi^n + b\nabla\pi^{n-1} + c\nabla\pi^{n-2}) \quad (6)$$

183 where  $\pi^n$  is unknown and should be obtained from the solution of an elliptic equation following

$$184 \quad \nabla(\rho\nabla\pi^n) = \frac{1}{a\Delta t^n} \nabla \cdot \rho\mathbf{u}^{**} - \frac{b}{a} \nabla(\rho\nabla\pi^{n-1}) - \frac{c}{a} \nabla(\rho\nabla\pi^{n-2}) \quad (7)$$

185 which is derived using the mass continuity constraint on the final velocity field:

$$\nabla \cdot \rho \mathbf{u}^{n+1} = 0 \quad (8)$$

It is important to realize that requiring  $\mathbf{u}^{**}$  to be zero at all sides of the cells inside an obstacle does not automatically mean that the final velocity  $\mathbf{u}^{n+1}$ , obtained from the pressure correction (6)-(7), will also be exactly zero; this is due to the inherently non-local nature of the elliptic equation for which the solution at a particular point depends simultaneously on the solution for the whole grid. However, as will be shown in Section 3d, the velocity field inside the obstacle is very small compared to the velocities right outside it. This outcome is explained by the fact that the pressure correction to the provisional velocity  $\mathbf{u}^{**}$ , to enforce continuity at each time step, is generally small. This is because the velocity change over a single time step is generally small, causing only a small divergence of the provisional momentum field to develop, which is precisely non-divergent at the beginning of each time step. The suppression of velocity inside obstacles can be further improved by iterating steps (5)-(7), which would make the final velocity  $\mathbf{u}^{n+1}$  after the pressure correction be a new provisional velocity  $\mathbf{u}^*$  to obtain the total solution (note that the solutions for pressure at each additional iteration should be added to the solution at previous iteration). Each additional iteration would add some additional computational expense to solving the elliptical equation (7). Obviously, the additional iterations only improve the solution inside the obstacles or near them and do not have any effect on the solution when obstacles are not present. As will be demonstrated in this study, the existence of small residual velocities does not seem to affect the simulated flow outside the obstacle in any significant manner; therefore, the iterations may not be even needed in most cases. This notion is consistent with results by Chen & Leach (2007), who compared an accurate solid-building approach to a simplified approach in which buildings are modeled by nudging the velocity to zero. A rather significant resultant nonzero residual flow occurred inside the buildings, but they also found a relatively small effect of such approximation on the external flow. Note that in some more traditional and accurate IBM approaches applied to anelastic or incompressible models, an expensive elliptic equation also needs to be solved at least twice on each time step (e.g., Zhang and Zheng, 2007).

### 3. Simulation of the flow around rectangular building

212

213 To test the performance of the QSBM in simulating the flow around solid obstacles, we performed  
214 two LES simulations for the case of a single rectangular building and compared it to the observational  
215 dataset from the Compilation of Experimental Data for Validation of Microscale Dispersion Models  
216 (CEDVAL; <https://mi-pub.cen.uni-hamburg.de/index.php?id=433>). We use reference cases from A1-1,  
217 which have been previously used for evaluation of other numerical models (e.g., Diehl et al., 2007; Gorlé  
218 et al., 2010; Trini Castelli & Reisin, 2010; Parente et al., 2011; Zhang et al., 2016). Specifically, we will  
219 use A1-1 to evaluate the velocity field and A1-5 to evaluate the dispersion of a gas tracer.

220

### 221 *a) Case setup*

222

223 The A1-1 setup aims to present a building that is 20 m long in the downwind direction, 30 m wide  
224 in the crosswind direction, and reaches a height ( $H$ ) of 25 m. In the wind tunnel, this setup is approximated  
225 with elements that are about 200 times smaller, counting on the fact that similarity arguments at very large  
226 Reynolds numbers allow one to extrapolate the results to the target building size. The scaling factor of  
227 200 is suggested by the CEDVAL and has been used by other models. In SAM, the building is represented  
228 on a Cartesian grid with a uniform grid-spacing of 1 m and domain size of 400 x 200 x 100 m in downwind  
229 ( $x$ ), crosswind ( $y$ ), and the vertical ( $z$ ) directions, respectively. The horizontal dimensions of the domain  
230 closely reproduce the wind tunnel's dimensions multiplied by the scale factor of 200 while the domain  
231 top corresponds to only about half of the height of the actual wind tunnel. The reduced extent of the  
232 domain top, relative to the wind tunnel, was deemed acceptable as preliminary tests have shown that the  
233 flow barely changes at the height of the domain top. In the SAM simulation, the building center is located  
234 in the domain center at coordinates  $x = 0$ ,  $y = 0$  with its base at  $z = 0$ .

235

236 The horizontal inflow wind velocity used in the simulations is specified using a simple power-law  
237 profile  $u(z) = U_{ref}(z/H_{ref})^a$ , which is suggested by the CEDVAL and closely approximates the  
238 observed inlet profile. The factor  $a$  is set to 0.21 for both the A1-1 and A1-5 simulations. Then for A1-1  
and A1-5, respectively, the reference height,  $H_{ref}$ , is set to 100 m and 125 m, and the reference windspeed,

239  $U_{ref}$ , is set to 6.0 and 5.85 m/s. In both simulations, the inflow wind is aligned along the x direction. Since  
240 SAM uses a periodic domain in that direction, strong nudging of the wind profile is applied in the first  
241 10% of the domain length (in the x direction) to maintain a close match to the specified inflow profile.  
242 Solid walls are placed at the four other sides of the domain to mimic the wind tunnel's walls. One caveat  
243 to mention is that the incoming flow in the CEDVAL experiments has been found to be somewhat  
244 turbulent with about a 20-30% turbulent intensity that is quite anisotropic, with horizontal turbulence  
245 having higher intensity than vertical turbulence. However, in our experiments we assume that the  
246 incoming flow is not turbulent as there is no clear way to initiate the required turbulence characteristics,  
247 which may have been caused by the particular construction of the wind-tunnel inlet. In terms of  
248 atmospheric stability, the temperature stratification is set to neutral to represent the wind-tunnel  
249 conditions.

250 The advection scheme used for all scalars is the fully three-dimensional monotonic and positive  
251 scheme MPDATA (Smolarkiewicz, 2006). The advection scheme for momentum is the second-order,  
252 centered-differences-in-flux form with conservation of kinetic energy. The surface everywhere is free-slip  
253 for simplicity, as at high Reynolds numbers (like in this case) the drag by the building surface does not  
254 have a large effect on the flow (it may affect the incoming profile near the surface, but we specify it). It  
255 might be important to use subgrid-scale (SGS) turbulent viscosity. However, for this case we tried both  
256 the Smagorinsky and 1.5-order closure for the SGS turbulence, based on prognostic SGS kinetic energy,  
257 and found little difference between the results.

258 To see the effect of additional iterations of the QSBM on the results and on the residual flow inside  
259 the building, three additional experiments were performed with one, two and three iterations. As will be  
260 discussed further, the number of iterations had small effect on overall results. Therefore, rather arbitrarily,  
261 most of the result will be presented using the simulation with two additional iterations.

262 Both simulations were run for 3900 s with a 0.05 s timestep. The first 900 steps are discarded as  
263 spin-up, so only the last 3000 s (i.e., 50-minutes) of each run are used for time averaging of the results.  
264 The averaging period is 750 times longer than characteristic time scale given by  $H/U_{ref}$  and, therefore,

265 more than sufficient to obtain a statistically steady solution. Even though this may seem to be a very long  
266 integration, for the wind-tunnel model of the building, which is 200 times smaller, this simulation time  
267 would correspond to about 15 seconds in the wind tunnel. Also note that because SAM is a parallel and  
268 efficient model, each simulation took only about an hour on a supercomputer using 200 cores; therefore,  
269 by any measure, it cannot be considered a “computationally expensive” simulation.

270

271 *b) Gas tracer release*

272

273 The QSBM allows for small “leaks” of momentum and kinetic energy into the obstacles which may  
274 not be problematic for most applications but may become a problem for advection of conserved scalars.  
275 Thus, simulating the dispersion of gas tracer releases requires one additional code modification: setting  
276 the flux of scalars through the obstacles’ boundaries to zero. In CEDVAL, the gas tracer is continuously  
277 released from four elongated openings at the bottom of the leeward wall of the building (representing four  
278 entrances to a parking garage) with a flow rate of 3 m/s; that is, they are not simple point sources. In SAM,  
279 these sources are simply modeled by four 3-grid-point continuous sources (i.e., 3 m) in the y direction  
280 right near the wall. Due to the constraint imposed on mass conservation in the incompressible model, it  
281 would be difficult to specify an additional flow of air, as in the actual gas tracer sources in CEDVAL. The  
282 absence of this additional flow may be responsible for some of the biases in the results. The CEDVAL  
283 dataset reports normalized gas tracer concentrations  $K$ , defined it as  $K = C \times U_{ref} \times H^2 / Q_s$ , where  $C$  is  
284 actual concentration and  $Q_s$  is total specified gas tracer release rate. This normalization process eliminates  
285 the need to produce a precise match between observed and simulated release rates such that an arbitrary  
286 release rate can be used in the model.

287

288 *c) Time-average flow*

289

290 The A1-1 dataset contains wind measurements for two planes, vertical at  $y/H=0$  (i.e., vertically  
291 through the center of the building) and horizontal at  $z/H=0.28$  (i.e., horizontally at 7 m above the base of  
292 the building). We begin by performing a qualitative evaluation of the main flow features in the planes as  
293 a whole, and then we offer a more qualitative evaluation in specific columns of the model.

294 Beginning with the vertical plane, Figure 1 illustrates the 50-min averaged flow streamlines  
295 (combined  $u$ ,  $w$  components) color coded by the wind speed in the wind tunnel (top panel) and in the  
296 simulation (bottom panel). Overall, the simulation captures well the main observed features of the flow  
297 around the building in this plane. In front of the building below the rooftop level, the flow separates into  
298 the so-called horseshoe vortex, where below  $\sim 2/3$  of the building height the flow dives towards the surface  
299 while above that height the flow rides upward and over the building rooftop. Both the observations and  
300 model show a rotation vortex upwind of the building face near the surface. That said, we note that the  
301 rotation center of the simulated vortex is farther away from the building than in observations. Over the  
302 rooftop of the building, a “separation bubble” develops, which is well reproduced by the model. In the  
303 building’s wake, a large leeside vortex is present, which, on this  $x$ - $z$  cross-section, is a visible part of a so-  
304 called “arch vortex” developing behind the building. The flow reverses direction in the low part of the  
305 leeside vortex, resulting in converging flow towards the building and rising flow along the leeside wall  
306 towards the rooftop. The position of the center of rotation of the leeside vortex is captured by the model  
307 quite well, albeit the simulated position is a bit higher than observed. Also, the simulated vortex extends  
308 as far as  $x/H = 1.9$  (47 m) in the simulation compared to  $x/H = 1.7$  (42 m) in the observations. We note  
309 that other models also have tended to overextend the leeside vortex in this CEDVAL case (e.g., Górlé et  
310 al., 2010; Trini Castelli & Reisin, 2010; Parente et al., 2011; Zhang et al., 2016).

311 Table 1 summarizes the comparison with the CEDVAL observations for the whole  $y/H=0$  plane  
312 as well as for three key zones shown in Figure 1, the windward zone (W), leeside zone (L), and the zone  
313 above the rooftop (R). Here we follow the methodology by Zhang et al. (2016). The mean relative error  
314 ( $RE$ ) of the wind velocity for the whole plane is 2.0% with an  $RMSE$  of 0.42 m/s; the overall spatial  
315 correlation with observations  $R = 0.97$ . As expected, the biggest challenge for the model is the leeside

316 flow, where the  $RE$  is the largest, 18.6%, and  $R = 0.91$ . The windward  $RE$  is rather small, 1.6% but,  
317 because of the error in the center position of the horseshoe vortex, the correlation is only 0.87. The flow  
318 over the rooftop is simulated the best, with  $RE = 0.7\%$  and  $R=0.98$ .

319 Moving on to the horizontal plane, Figure 2 illustrates the 50-min averaged flow streamlines  
320 (combined  $u$ ,  $v$  components) color coded by the wind speed in the wind tunnel (top panel) and in the  
321 simulation (bottom panel). Again, the main characteristics of the flow in that plane are well reproduced  
322 by the model. Those include the “separation bubbles” at the building’s sides that consist of two  
323 counterrotating vortices and the position of rotation centers at the leeside of the building. This pair of  
324 vortices at the leeside is also a part of the arch vortex. The acceleration of the flow around the building  
325 corners is well reproduced not only qualitatively, but also quantitatively.

326 Table 2 summarizes the statistics of the flow for the whole  $z/H=0.28$  plane as well as separately  
327 for three key zones shown in Figure 2, the windward zone (W), the zone across the lateral walls (S), and  
328 leeside zone (L). For the whole plane,  $RE = 9.4\%$  and  $R=0.91$ . The largest  $RE = 16.1\%$  is found in the  
329 front of the building with  $R=0.93$ . The overall leeside flow is reproduced better, with  $RE= 10.2\%$  and  
330  $R=0.92$ . Despite the fact that the model performs better in the zone across the lateral walls in terms of the  
331 mean wind with  $RE = 7.1\%$ , the spatial correlation of the wind velocity is only  $R = 0.86$ . Overall, our  
332 statistical results summarized by Tables 1 and 2 are quite close to the results presented by Zhang et al.  
333 (2016).

334 Figures 3 and 4 offer another way of evaluating the simulated flow in the same planes as the  
335 previous figures. In addition, these figures present results obtained for using different number of iterations  
336 of the QSBM whereas Figures 1 and 2 only show results using 2 iterations.

337 Beginning with the vertical plane, Figure 3 shows vertical profiles of the 50-min mean horizontal  
338 (along the  $x$  axis;  $u$ ) and vertical ( $w$ ) velocities at various distances from the building center along the  $x$   
339 axis at  $y/H = 0$  (i.e., along the direction of the wind passing through the center of windward and leeward  
340 building faces). As mentioned above, the main inconsistency with the observations is that the horseshoe  
341 vortex near the surface is relatively farther upstream from the building, as evident by the velocity profiles

342 at  $x/H = -1$ . Closer to the windward wall ( $x/H = -0.6$ ), the magnitude of both downward and upward vertical  
343 velocities and the position of the stagnation point ( $w = 0$ ) are reproduced quite well, although  $w$  near the  
344 rooftop level is overestimated by about 1 m/s. Both profiles above the rooftop at the building's center  
345 ( $x/H=0$ ) are reproduced very well. The profiles through the leeside vortex ( $x/H = 0.6$  and  $x/H = 1$ ) also  
346 show good agreement with the observations. One can clearly see the reverse return flow towards the  
347 building throughout most of the building height. The profile of the mean wind in the building's wake at  
348  $x/H = 3$ , which is relatively far away from the flow reconnection point, is also well reproduced.

349 Moving on to the horizontal plane, Figure 4 shows horizontal profiles of  $u$  and  $v$  at various  
350 distances from the building center along the  $x$  axis at  $z/H = 0.28$ . Overall, the profiles are reproduced quite  
351 well by the model. There is a slight underestimation of the incoming velocity in front of the building at  
352  $x/H=-0.6$ . Also, there are two “kinks” in the corresponding  $v$  profile in front of the building corners at the  
353 distance of  $\pm 0.7$  from the center line, which can be explained by some noise generated by the second-order  
354 advection scheme for momentum because of the sharp corners of the building. The acceleration of the  
355 flow and the flow towards the building near its side walls at  $x/H=0$  is in good agreement with observations.  
356 In the leeside, at  $x/H=0.6$  and  $x/H=1.0$ , the magnitude of the return flow towards the building is reproduced  
357 very well, although the downwind velocity outside of the return flow is clearly underestimated. The  
358 profiles of the reconnected flow at  $x/H=3.0$  is also well reproduced.

359

#### 360 *d) Residual flow inside the building*

361

362 The results shown in Figures 3 and 4 indicate that the number of iterations used in the QSBM have  
363 only a minor impact on the mean flow. For completeness, we explore their impact on the residual flow  
364 inside the building. Figure 5 shows the 50-min mean horizontal (along the  $x$  axis;  $u$ ) and vertical ( $w$ )  
365 velocities or “residual velocities” in the vertical plane  $y/H = 0$  (i.e., along the direction of the wind passing  
366 through the center of windward and leeward building faces) for simulations relying on various numbers  
367 of iterations in the QSBM. When no iterations are performed, the maximum residual velocity inside the

368 building is about 0.1 m/s at the upper inflow corner. The largest standard deviation of the residual velocity  
369 is smaller than 0.005 m/s (not shown). Considering that the inflow wind is several meters-per-second, it  
370 is fair to say these residual velocities are already quite small. Each iteration further reduces the residual  
371 velocity by about a factor of two; so after two and three iterations, the maximum residual velocities in the  
372 plane decrease to about 0.02 and 0.01 m/s, respectively. In terms of computational expense, the bi-  
373 directional-FFT pressure solver takes about 20% of running time in the particular parallel model  
374 configuration running on 200 CPUs, so each additional iteration adds about 20% to the expense.

375

376 *e) Turbulence*

377

378 So far, we have presented time averaged results. It is also important to see the ability of the model  
379 to simulate the turbulence associated with the flow around a building. As was mentioned above, the  
380 incoming flow in the simulation is not turbulent, but the incoming flow in the wind-tunnel experiment  
381 already has some turbulence, especially in the  $u$ -component. There is no simple way to initialize the  
382 anisotropic turbulence in the model to mimic the turbulence at the inlet of the wind tunnel. The turbulent  
383 kinetic energy of the incoming flow would contribute some additional turbulence behind the building, and  
384 this factor is absent in the simulation. However, most of turbulence is generated by the building itself;  
385 therefore, with the aforementioned caveat in mind, we will still compare the turbulent intensities produced  
386 by the model against the observations.

387 Figure 6 compares the turbulent intensity, or the standard deviation of turbulent wind velocity  
388 fluctuations, individually for each of the wind components in the vertical symmetry plane  $y/H = 0$ .  
389 Unfortunately, only turbulent intensities for the  $u$  and  $w$  components of the wind are reported in that plane  
390 by the CEDVAL A1-1 dataset. The region with maximum turbulence is just above the building rooftop in  
391 both the simulations and observations. On the leeward side, the turbulence is relatively weak immediately  
392 behind the building within the distance approximately equal to the building's height, as in observations.  
393 The highest levels of turbulent intensity of the  $u$  component are generally above the building's rooftop

394 height as observed. On the contrary, the maximum intensity of the  $w$ -component is generally below the  
395 rooftop height mostly above the upper half of the building. Overall, the spatial structure of the turbulent  
396 regions behind in the wake of the building is well reproduced by the model.

397

398 *f) Gas tracer transport*

399

400 Figure 7 shows normalized gas tracer concentration in the vertical plane at  $y/H=0$ . The greatest  
401 concentrations are found near the ground close to the leeside wall, where the sources are. In the simulation,  
402 the gas tracer concentration reaches a maximum of 56.3 normalized units vs the 66.7 normalized units in  
403 the wind tunnel. The gas tracer is transported by the leeside vortex up along the leeward wall towards the  
404 rooftop, where it gets swept into the “separation bubble” above the rooftop. Overall, the model seems to  
405 reproduce the observed distribution of concentration rather well, especially throughout the leeside vortex,  
406 but tends to underestimate concentration above the rooftop.

407 Figure 8 shows normalized gas tracer concentration in horizontal planes at  $z/H = 0.08$  (2 m) and  
408  $z/H = 0.28$  (7 m). Overall, the horizontal distribution of gas tracer concentration at the leeside is reproduced  
409 quite satisfactory in both horizontal planes. The main model biases are within the “separation bubbles”  
410 along the side walls of the building, like the one over the rooftop, where concentration is also  
411 underestimated. Nevertheless, the gas tracer seems to penetrate all the way to the front corners of the  
412 building, like in observations. The apparent difficulty that the model has with the cavities along the side  
413 walls and over the rooftop can be attributed to the flow being rather unresolved there, as the thickness of  
414 the “bubbles” (see Figures 1 and 2) are only several grid cells. Also, as mentioned before, the sources of  
415 gas tracers in the wind-tunnel experiment are not point sources but, rather, are jets ejecting gas tracer with  
416 the speed of 3 m/s from four elongated openings in the leeward building’s wall. It is not clear how to  
417 mimic such dynamic sources of gas tracers in SAM.

418

#### 419 **4. Simulations of obstacles not aligned with the grid**

420

421 In the previous section, we reported the results of flow around an idealized rectangular building  
422 when the boundaries are perfectly aligned with the grid cells' boundaries which, arguably, is an ideal  
423 situation for testing our method. However, an important question remains as to how universal the proposed  
424 method is when applied to obstacles with boundaries that are not aligned with the numerical grid. To  
425 answer this question, we apply the QSBM method to two other cases. In the first case, we simulate the  
426 flow around a building in a shape of a cube rotated  $45^\circ$  relative to the flow and also to the grid; i.e., with  
427 its corner facing the incoming flow. In the second case, we consider flow around a building in the form of  
428 a circular cylinder with a height/diameter ratio of one. In each case, an obstacle is represented by a  
429 population of whole grid cells that fit inside its actual geometric boundaries.

430

431 *a) A cubic building rotated  $45^\circ$*

432

433 This test is based on the CEDVAL A1-6 case of a cube rotated  $45^\circ$  relative to the direction of the  
434 incoming flow. In the dataset, the size scaling factor of 200 is also suggested, so the cubic building has  
435  $H=25$  m size for all dimensions. The incoming flow profile is the same as in A1-1 case. The model grid  
436 and duration of the run are also identical to our simulation of the A1-1 case. Figure 9 compares model to  
437 observations, showing the wind vectors at the  $y/H=0$  symmetry plane and horizontal cross-section at the  
438  $z/H=0.4$  height. Note that, unlike the A1-1 case, the measurements of the wind in A1-6 case were relatively  
439 sparse. In the figure, all the available data are plotted, with model results shown at the same locations as  
440 the measurements. One can see that in the case of rotated cube, there is a clear horse-shoe vortex does not  
441 develop upstream from the building as was the case in A1-1. There is also virtually no acceleration of the  
442 flow above the building and no indication of the separation bubble developing over the roof. The bulk of  
443 the flow seems to prefer to go around the building's side corners rather over the top of the building. The  
444 model seems to capture this behavior rather well, both qualitatively and quantitatively. In the leeside of  
445 the building, the arch-vortex also develops, with a leeside vortex and associated reverse flow towards the  
446 building clearly visible in the vertical cross-section. The leeside extent of the flow seems to be somewhat

447 overestimated in the simulation, as in the A1-1 case, but it is difficult to quantify that difference due to  
448 the sparsity of observations. Similar to the A1-1 case, there is a pair of vortices behind the building (only  
449 one of them is actually shown), clearly visible in the horizontal cross-section. The model seems to shift  
450 the center of rotation further downstream than in observations, probably because of the rather rough  
451 representation of the building walls in this case when the grid is not aligned with the building surfaces.

452 Tables 3 and 4 present statistics of comparisons with the CEDVAL observations for  $y/H=0$  and  
453  $z/H=0.4$  planes, respectively, for windward zone (W) and leeside zone (L) shown in Fig. 9 as well as for  
454 all observations for a given plane. For the vertical  $y/H=0$  plane, the  $RE$  of the wind velocity is 7.6% with  
455 an  $RMSE$  of 0.42 m/s and  $R = 0.96$ . The biggest challenge for the model is before is the leeside flow,  
456 where the  $RE$  is the largest, 9.3%, and  $R = 0.94$ . The windward  $RE$  is also relatively large, 6.2%, but the  
457 correlation is very high 0.99. The flow over the rooftop is simulated the best, with  $RE = 0.7%$  and  $R=0.98$ .  
458 For the horizontal  $z/H=0.28$  plane as the whole,  $RE = 6.1%$  and  $R=0.91$ . The largest  $RE = 13.5%$  is found  
459 again in the leeside zone with  $R=0.89$ , while the windward zone is simulated much better with  $RE = 4.2%$   
460 and  $R=0.94$ . Overall, we may conclude that the flow in this case of rotated cubic building is simulated  
461 reasonably well.

462

#### 463 *b) A flow around a circular cylinder*

464

465 To further investigate the ability of our method to simulate the flow around obstacles that have  
466 boundaries not aligned with the Cartesian grid, we simulate the flow around a circular cylindrical building  
467 with the aspect ratio (ratio of height to diameter) of one. We use the setup from an LES study by Kumar  
468 and Tiwari (2021; further KT21), which, in turn, is based on the experimental and LES results reported  
469 by Pattenden et al (2007; further P07). The latter used a structured grid conformal to the cylinder shape,  
470 while the former used the conventional IBM on a Cartesian grid. In KT21, the incoming wind profile was  
471 obtained first by a separate LES simulation of a neutral surface layer over a flat surface with a given  
472 roughness length  $z_o$ . It was found that the resultant profile is very close to a log-law profile

473  $u(z) = \frac{u_*}{k} \ln \frac{z}{z_o}$ , where  $u_*=0.29$  m/s,  $z_o=0.046$  m, and  $k$  is von Karman constant. In KT21, the height of  
474 the cylinder is 4 m. We scaled up the size of the cylinder by a factor of 10 to  $H=40$  m, which would be a  
475 more reasonable size for a building. To maintain the self-similarity of the flow, a factor of 10 increase was  
476 also applied to the roughness length in the specified log-law wind profile, yielding  $z_o = 0.46$  m. The grid  
477 spacing was also increased to 1 m from the 0.1 m in KT21, to preserve the relative grid resolution of the  
478 cylinder. The numerical domain is chosen to be the same in the horizontal directions as in the previous  
479 runs, but the domain is twice as tall because the building is also taller than before. The time step and run  
480 duration were the same as in the previous runs.

481 Figure 10 illustrates the overall structure of the time-averaged flow around the cylinder showing  
482 velocity vectors in the vertical plane through the center of the cylinder as well as in the horizontal plane  
483 at cylinder's mid-height. Overall, all the features that we saw in the case of rectangular building are  
484 present, namely: a horse-shoe vortex in front of the cylinder, an arch-vortex in the leeside with the return  
485 flow towards the cylinder in its wake with a pair of counterrotating vortexes, and the separation "bubble"  
486 over its top. The flow features are consistent with the results presented by KT21 (see their Figs 5 and 6).  
487 However, there are some clear differences. Similar to the simulation of the rectangular building, the horse-  
488 shoe vortex is overextended upstream with the position of separation point near the surface at  $x/H = -2$   
489 compared to the observed  $x/H = -1$  given in P07. This is probably due to our use of free-slip conditions  
490 and insufficient vertical resolution near the surface. Note that the position of the separation point is also  
491 overextended in KT21 ( $x/H = -1.5$ ) and LES results by P07 ( $x/H = -1.45$ ). The height of the stagnation  
492 point, where the separation of the incoming flow into upward and downward branches occurs at the  
493 upstream surface of the cylinder, is at  $z/H = 0.7$ , which is close to  $z/H = 0.65$  reported by KT21. The  
494 surface position of the flow reattachment point of the leeside vortex is also overextended at about  $x/H =$   
495  $2.2$ , compared to the observed  $x/H = 1.6$ . However, the KT21 and P07 studies also had difficulty  
496 reproducing this parameter, reporting  $x/H = 1.95$  and  $x/H = 2.1$ , respectively. On the top of the cylinder,  
497 the reattachment of the separated flow is at  $x/H = 0.35$ , same as in KT21 and close to  $x/H = 0.39$  in P07.

498 It is rather common when modeling the flow around blunt objects, such as a cylinder, to look at a  
499 so-called pressure coefficient:  $C_p = (p - p_\infty) / \frac{1}{2} \rho V_\infty^2$ , where  $p$  is the pressure on the object's surface,  $\rho$  is  
500 air density,  $p_\infty$  and  $V_\infty$  are the pressure and velocity upstream of the flow far from the object. In the case  
501 of a cylinder, the pressure coefficient is measured along its surface at some fixed height as a function of  
502 the angle  $\Phi$  in cylindrical coordinates relative to the cylinder's center, usually between  $\Phi = 0^\circ$  and  $\Phi =$   
503  $180^\circ$  which is between upstream and downstream points of the cylinder's surface. Figure 11 compares  $C_p$   
504 at  $z/H = 0.5$  to the modeling and experimental results presented by P07 superimposing our results on their  
505 Fig. 7. One can see that overall, the distribution of pressure coefficient near the cylinder's surface is  
506 captured rather well by SAM. Some apparent noisiness of the SAM results is associated with the rather  
507 rough approximation of the curved cylinder surface by rectangular cells in our method. We can also use  
508 the pressure coefficient to compute the drag coefficient  $C_D$ , which, in case of a cylinder, is computed as  
509  $C_D = \int_0^\pi C_p \cos \Phi d\Phi$  (e.g., Bertin 2002). From our results, we obtain the drag coefficient to be 0.82, which  
510 is close to the observed value of 0.79 reported by P07.

511

## 512 **5. Summary**

513

514 In this paper, we present a method for incorporating obstacles, such as buildings, into SAM. This  
515 model is usually used to address climate-related questions but can be also employed as an LES model to  
516 answer emerging urban microclimate questions. The method, which we call the Quasi-Solid Box Method  
517 (QSBM), can be considered to be a subset of the immersed-boundary method (IBM), called the force-  
518 body methods, that stagnate the flow everywhere inside an obstacle. Unlike some other force-body  
519 methods that use fictitious damping or relaxation terms in the momentum equations, the QSBM avoids  
520 them by explicitly setting the provisional velocity components to zero in the cells that are inside an  
521 obstacle, right before applying the pressure-gradient terms to enforce non-divergence of the flow.

522 We tested the method using a case of a flow past an idealized single rectangular building in neutral  
523 atmospheric conditions and compared the results to the CEDVAL wind-tunnel observations. Overall, the

524 model performance in this case can be considered satisfactory. All major flow features are well  
525 reproduced, such as the existence of an arch vortex in lee of the building, the horseshoe vortex and the  
526 height of the separation point of the inflow in front of the building, and the “separation bubbles” over the  
527 rooftop and on building sides. The model has a difficulty, though, reproducing the exact position of the  
528 center of rotation of the horseshoe vortex and tends to overestimate slightly the extent of the leeside vortex.  
529 On the other hand, the vertical wind structure of the flow above the rooftop and downstream from it is  
530 reproduced quite well, particularly the strength of the return flow towards the leeside wall. The highest  
531 levels of turbulence are simulated above the building rooftop, in accord with observations. A relatively  
532 calm zone, with relatively low levels of turbulence, is found behind the building within the distance  
533 approximately equal to the building’s height, also as in observations.

534         The QSBM allows a residual flow inside the obstacles that is very small compared to the magnitude  
535 of velocity in its vicinity; however, the residual velocities can be further reduced by iterating over the last  
536 steps that enforce zero velocity and non-divergence of the flow. The added expense is about 20% increase  
537 of running time per each additional iteration. In this study, each additional iteration would reduce the  
538 maximum magnitude of residual velocities inside the building by about a factor of two. However, overall,  
539 the use of iterations makes only a minor improvement over the simulation with no iterations. This  
540 conclusion might not be generalizable, so, ideally, sensitivity of the results to at least a single iteration  
541 should be tested when the method is employed to simulate other cases.

542         We additionally evaluate the ability of this method to handle the dispersion of gas tracers. The gas  
543 tracer dispersion also agrees rather well with observations, although some challenges remain in  
544 reproducing transport of gas tracer into the “separation bubbles”, not only over the rooftop, but also along  
545 its crosswind sides.

546         One of the drawbacks of the QSBM is that it requires approximation of any obstacle as a collection  
547 of whole grid cells that fit inside the obstacle’s actual geometric boundaries. This was not a problem in  
548 our simulation of a rectangular building as, in this case, the grid-cell boundaries conform to the building’s  
549 boundaries perfectly. However, in the case of a city, simulated buildings may not conform to the grid-cell

550 boundaries; so, as a result, they may have staircase-like walls. To evaluate the performance of the method  
551 in such cases, we presented the results of two additional simulations. The first is based on another  
552 CEDVAL case of the flow around a cubic building rotated by  $45^\circ$  to the direction of the incoming flow;  
553 the second case is for a cylindrical building with the aspect ratio of one, obtained from a different  
554 observational dataset and to which our results are compared to published results from two other LES  
555 models. Overall, the rotated building results compare rather well to the wind tunnel observations, both  
556 qualitatively and quantitatively. The biggest bias was in the exact position of the arch-vortex and some  
557 overextension of the leeside-vortex. In the case of the flow around the cylindrical building, all major  
558 observed features of such a flow have been fairly well represented by the model. Some notable biases are  
559 found, such as the position of a horse-shoe vortex and the extent of the leeside vortex. However, these  
560 biases are generally similar to those shown by other LES models for this case, which can be the indication  
561 of some fundamental difficulties in simulating such obstacles that are not necessarily SAM-specific.  
562 Despite the biases in the position of vortices, the angular distribution of a pressure coefficient around the  
563 cylinder and closely related aerodynamic drag coefficient have been well simulated by SAM when  
564 compared to actual measurements.

565 Overall, we find the results of the tests reported in this study to be quite encouraging. However,  
566 we caution that the QSMB should not be viewed as computationally inexpensive alternative to a more  
567 comprehensive and accurate traditional IBM. We implemented this method in SAM primarily to be able  
568 to simulate the turbulence and tracer transport around a city in the planetary boundary layer, when the  
569 buildings are relatively coarsely represented due to the computational cost. For such problems, the QSMB  
570 becomes a very attractive approach as its implementation requires very minor code modifications without  
571 affecting the computational efficiency of SAM.

572

573 **Acknowledgements.** This work was supported by the Brookhaven National Laboratory under its  
574 Laboratory Directed Research and Development (LDRD) Program, Project #20-002. This research used  
575 resources of the National Energy Research Scientific Computing Center; a DOE Office of Science User  
576 Facility supported by the Office of Science of the U.S. Department of Energy under Contract No. DE-

577 AC02-05CH11231. All model output used in this study is accessible through NCAR Campaign Storage  
578 via Globus.

579

580

581

## References

582

583 Bertin J.J. (2002). *Aerodynamics for Engineers*, 4<sup>th</sup> edition, Prentice Hall.

584 Blocken, B. (2018). LES over RANS in building simulation for outdoor and indoor applications: A  
585 foregone conclusion? *Building Simulation*, 11(5), 821–870.

586 Chan, S. T., & Leach, M. J. (2007). A validation of FEM3MP with Joint Urban 2003 data. *J. Appl. Meteor.  
587 and Clim.*, 12, 2127–2146.

588 Diehl, S.R., Burrows, D.A., Hendricks, E.A., & Keith, R. (2007). Urban dispersion modeling: Comparison  
589 with single-building measurements. *J. Appl. Meteor. Climatol.*, **46**, 2180–2191.

590 Duran, D. R. (1991). The Third-Order Adams-Bashforth Method: An Attractive Alternative to Leapfrog  
591 Time Differencing. *Mon. Wea. Rev.*, 119(3), 702-720.

592 Fortunato, A. B., and A. M. Baptista, 1996: Evaluation of horizontal gradients on sigma coordinate  
593 shallow water models. *Atmos. Ocean* 34, 489-514.

594 Gal-Chen, T., & Somerville, C.J. (1975). On the use of a coordinate transformation for the solution of the  
595 Navier–Stokes equations. *J. Comput. Phys.*, 17, 209–228.

596 Gorlé, C., van Beeck, J., & Rambaud, P. (2010). Dispersion in the Wake of a Rectangular Building:  
597 Validation of Two Reynolds-Averaged Navier–Stokes Modelling Approaches. *Boundary-Layer  
598 Meteorol.*, **137**, 115–133. <https://doi.org/10.1007/s10546-010-9521-0>

599 Hanna, S., and Coauthors, 2006: Detailed simulations of atmospheric flow and dispersion in downtown  
600 Manhattan: An application of five computational fluid dynamics models. *Bull. Amer. Meteor. Soc.*,  
601 87, 1713–1726.

602 Iaccarino, G., and R. Verzicco, (2003). Immersed boundary technique for turbulent flow simulations.  
603 *Appl. Mech. Rev.*, 56, 331–347.

604 Khairoutdinov, M. F., & Randall, D.A. (2003). Cloud-resolving modeling of the ARM summer 1997 IOP:  
605 Model formulation, results, uncertainties, and sensitivities. *J. Atmos. Sci.*, 60, 607-625.

606 Korycki, M; Loboeki, L, and Wyszogrodzki, A, 2016: Numerical simulation of stratified flow around a  
607 tall building of a complex shape. *Environ. Fluid Mech*, 16(6), 1143-1171.

608 Kumar P. and Tiwari, S. (2021): Effects of size ratio and inter-cylinder spacing on wake transition in flow  
609 past finite inline circular cylinders mounted on plane surface, *Physics of Fluids*, 33, 023602  
610 <https://doi.org/10.1063/5.0037712>

611 Lundquist, K. A., F. K. Chow, and J. K. Lundquist (2010): An immersed boundary method for the  
612 Weather Research and Forecasting Model. *Mon. Wea. Rev.*, 138, 796–817, [https://](https://doi.org/10.1175/2009MWR2990.1)  
613 [doi.org/10.1175/2009MWR2990.1](https://doi.org/10.1175/2009MWR2990.1).

614 Lundquist K.A., Chow F.K., Lundquist J.K. (2012) An immersed boundary method enabling large-eddy  
615 simulations of flow over complex terrain in the WRF model. *Mon Wea Rev* 140, 3936–3955.  
616 <https://doi.org/10.1175/MWR-D-11-00311.1>

617 Muñoz-Esparza, D., Sauer, J. A., Shin, H. H., Sharman, R., Kosović, B., Meech, S., et al. (2020).  
618 Inclusion of building-resolving capabilities into the FastEddy® GPU-LES model using an immersed  
619 body force method. *J. of Adv. in Model. Earth Sys.*, 12, e2020MS002141. [https://](https://doi.org/10.1029/2020MS002141)  
620 [doi.org/10.1029/2020MS002141](https://doi.org/10.1029/2020MS002141)

621 Mittal, R., & Iaccarino, G. (2005). Immersed Boundary Methods. *Ann. Rev. of Fluid Mech.*, 37, 239–261.

622 Parente, A., Górlé, C., van Beeck, J., & Benocci, C. (2011). Improved k-ε model and wall function  
623 formulation for the RANS simulation of ABL flows. *Journal of Wind Engineering and Industrial*  
624 *Aerodynamics*, 99, 267–278.

625 Pattenden, R. J., N. W. Bressloff, S. R. Turnock, and X. Zhang, (2007): Unsteady simulations of the flow  
626 around a short surface-mounted cylinder. *Int. J. Numer. Methods Fluids*, 53, 895–914.

627 Profiroiu, C. M., Bodislav, D. A., Burlacu, S., & Rădulescu, C. V. (2020). Challenges of Sustainable  
628 Urban Development in the Context of Population Growth. *European Journal of Sustainable*  
629 *Development*, 9, 3, 51-57. doi: 10.14207/ejsd.2020.v9n3p51

630 Smolarkiewicz, P.K. (2006). Multidimensional positive definite advection transport algorithm: an  
631 overview. *Int. J. Numer. Methods Fluids*, 50, 1123–1144.

632 Smolarkiewicz, P. K., Sharman, R., Weil, J., Perry, S. G., Heist, D., & Bowker, G. (2007). Building  
633 resolving large-eddy simulations and comparison with wind tunnel experiments. *Journal of*  
634 *Computational Physics*, 227(1), 633–653.

635 Trini Castelli, S., & Reisin, T.G. (2010). Evaluation of the atmospheric RAMS model in an obstacle  
636 resolving configuration. *Environ Fluid Mech.*, **10**, 555–576. [https://doi.org/10.1007/s10652-010-](https://doi.org/10.1007/s10652-010-9167-y)  
637 [9167-y](https://doi.org/10.1007/s10652-010-9167-y)

638 Zhang, N., Du, Y., & Miao, S. (2016). A microscale model for air pollutant dispersion simulation in urban  
639 areas: Presentation of the model and performance over a single building. *Adv. Atmos. Sci.*, **33**, 184–  
640 192. <https://doi.org/10.1007/s00376-015-5152-1>

641 Zhang, N., and Z.C. Zheng (2007): An improved direct-forcing immersed-boundary method for finite  
642 difference application. *J. Comp. Phys.*, 221, 2250-268.

643

644

645 **Tables**

646 **Table 1** Comparison of CEDVAL A1-1 observations and simulation for the whole plane  $y/H=0$  and for zones shown  
 647 in Figure 1 for mean ( $MN$ ), absolute error ( $E = MN_{sim}-MN_{obs}$ ), relative error ( $RE=|E/ MN_{obs}|$ ), root-mean-square  
 648 error (RMSE), and correlation coefficient ( $R$ ).

Zone	$MN_{obs}(m/s)$	$MN_{sim}(m/s)$	$E (m/s)$	$RE$	$RMSE (m/s)$	$R$
W - Windward	2.59	2.63	0.04	1.6%	0.60	0.87
L - Leeseide	1.41	1.14	-0.26	18.7%	0.47	0.91
R - Rooftop	4.58	4.61	0.03	0.7%	0.29	0.98
$y/H=0$	3.28	3.22	-0.06	2.0%	0.42	0.97

649  
 650 **Table 2** Comparison of CEDVAL A1-1 observations and simulation for the whole plane  $z/H=0.28$  and for the zones  
 651 shown in Figure 2 for mean ( $MN$ ), absolute error ( $E = MN_{sim}-MN_{obs}$ ), relative error ( $RE=|E/ MN_{obs}|$ ), root-mean-  
 652 square error (RMSE), and correlation coefficient ( $R$ ).

Zone	$MN_{obs}(m/s)$	$MN_{sim}(m/s)$	$E (m/s)$	$RE$	$RMSE (m/s)$	$R$
W - Windward	2.51	2.11	-0.40	16.1%	0.50	0.93
L - Leeseide	2.48	2.23	-0.25	10.2%	0.53	0.92
S - Sides	3.42	3.18	-0.24	7.1%	0.79	0.86
$z/H=0.28$	2.81	2.55	-0.26	9.4%	0.55	0.91

653  
 654 **Table 3** Comparison of CEDVAL A1-6 observations and simulation for the whole plane  $y/H=0$  and for the zones  
 655 shown in Figure 9 for mean ( $MN$ ), absolute error ( $E = MN_{sim}-MN_{obs}$ ), relative error ( $RE=|E/ MN_{obs}|$ ), root-mean-  
 656 square error (RMSE), and correlation coefficient ( $R$ ).

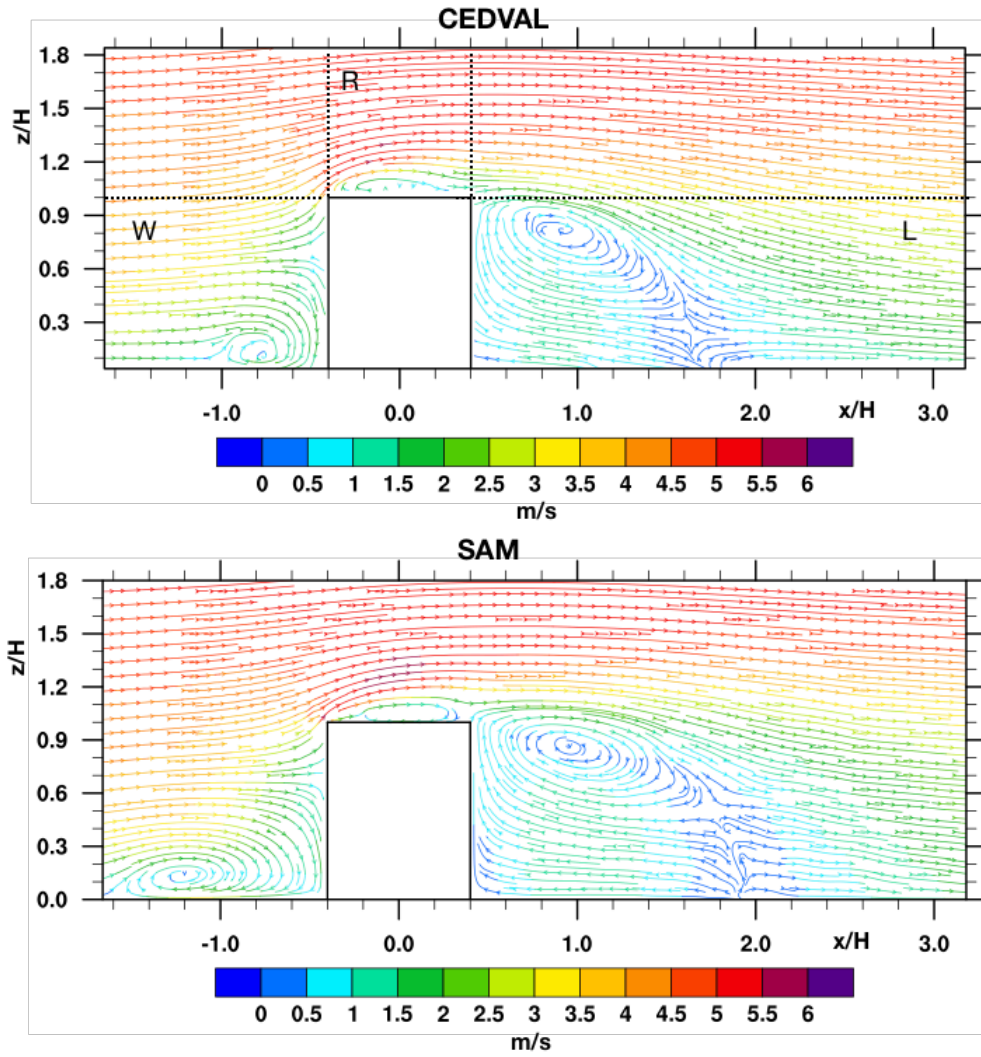
Zone	$MN_{obs}(m/s)$	$MN_{sim}(m/s)$	$E (m/s)$	$RE$	$RMSE (m/s)$	$R$
W - Windward	3.23	3.43	0.2	6.2%	0.23	0.99
L - Leeseide	2.98	3.25	0.27	9.3%	0.55	0.94
$y/H=0$	3.21	3.45	0.24	7.6%	0.42	0.96

657  
 658 **Table 4** Comparison of CEDVAL A1-6 observations and simulation for the whole plane  $z/H=0.4$  and for the zones  
 659 shown in Figure 9 for mean ( $MN$ ), absolute error ( $E = MN_{sim}-MN_{obs}$ ), relative error ( $RE=|E/ MN_{obs}|$ ), root-mean-  
 660 square error (RMSE), and correlation coefficient ( $R$ ).

Zone	$MN_{obs}(m/s)$	$MN_{sim}(m/s)$	$E (m/s)$	$RE$	$RMSE (m/s)$	$R$
W - Windward	2.42	2.52	0.1	4.2%	0.23	0.94
L - Leeseide	1.81	1.56	-0.24	13.5%	0.57	0.89
$z/H=0.4$	2.08	1.95	-0.13	6.1%	0.44	0.91

661  
 662  
 663  
 664 **Figures**

666

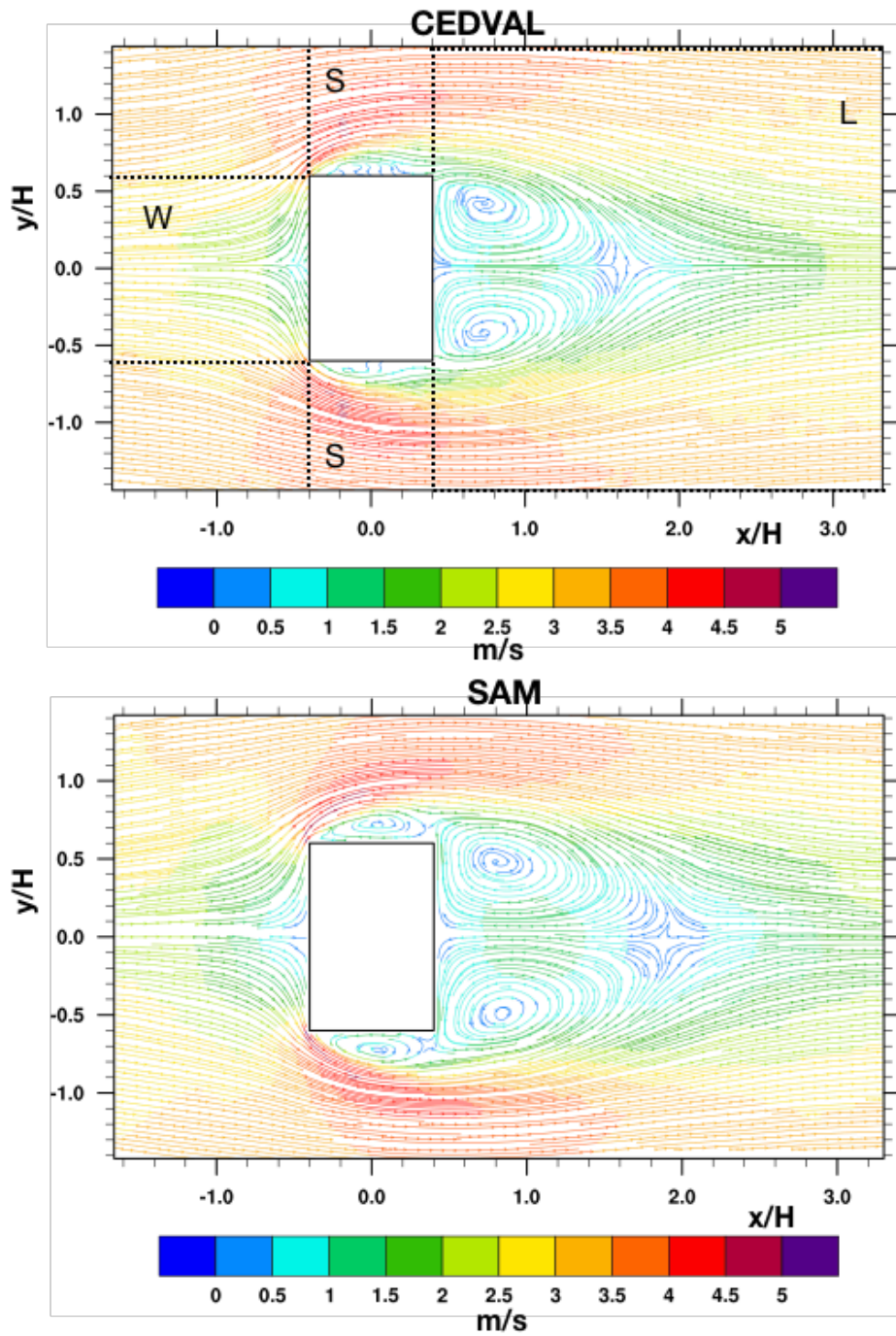


667

668

669

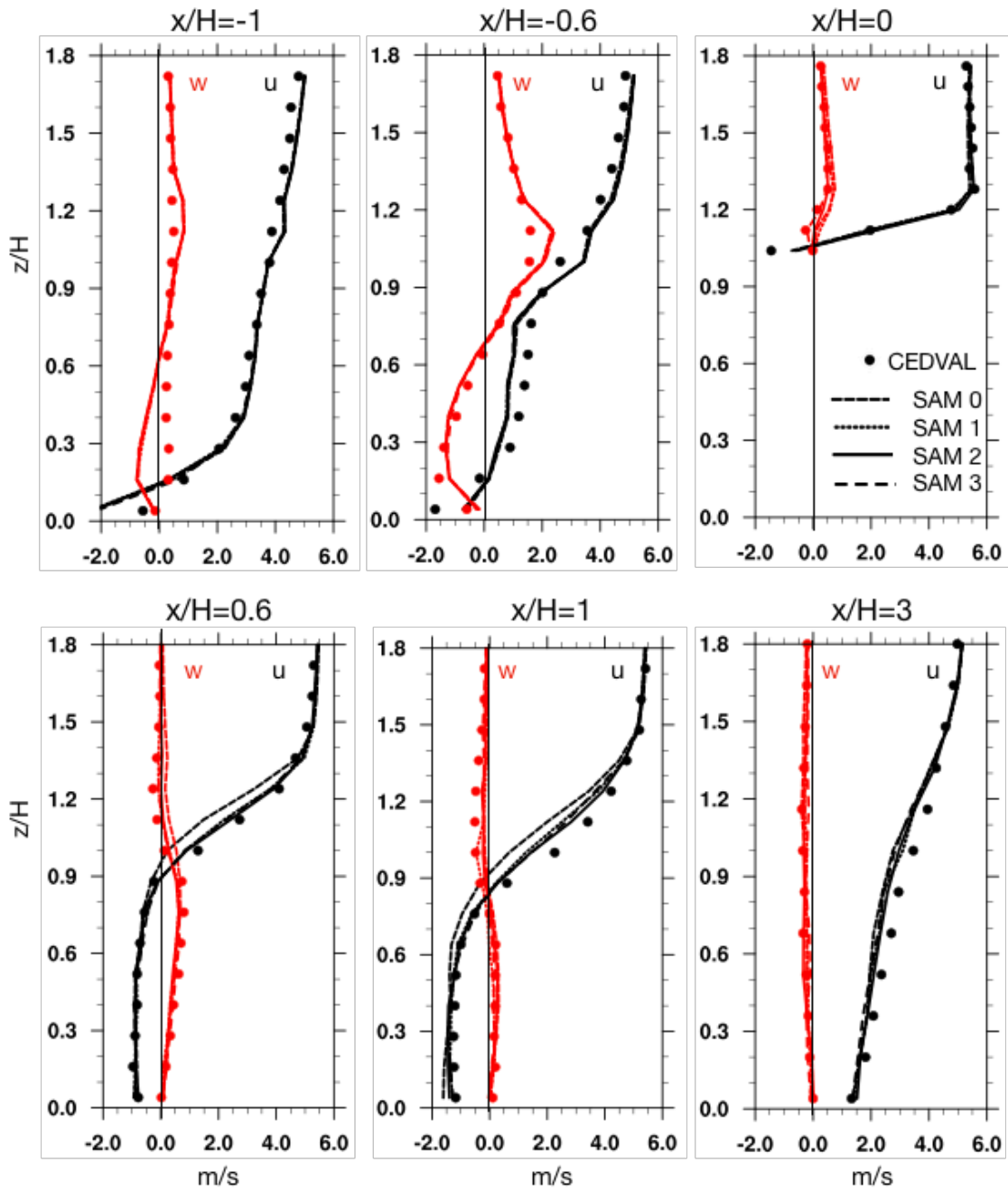
**Figure 1.** Vertical cross-section of wind at  $y/H = 0$  for CEDVAL observations (top) and SAM simulation (bottom). The coordinates are normalized by height of the building. The dashed lines in the top plot indicate the boundaries of the key zones used for statistical comparison: W – windward in front of the building; R – above the rooftop; L – leeside vortex and wake zone.



670

671

**Figure 2.** Horizontal cross-section of wind at  $z/H = 0.28$  for CEDVAL observations (top) and SAM simulation (bottom). The coordinates are normalized by height of the building. The dashed lines in the top plot indicate the boundaries of the key zones used for statistical comparison: W – windward in front of the building; S – across from lateral side walls; L – leeward vortices and wake zone.



672

673

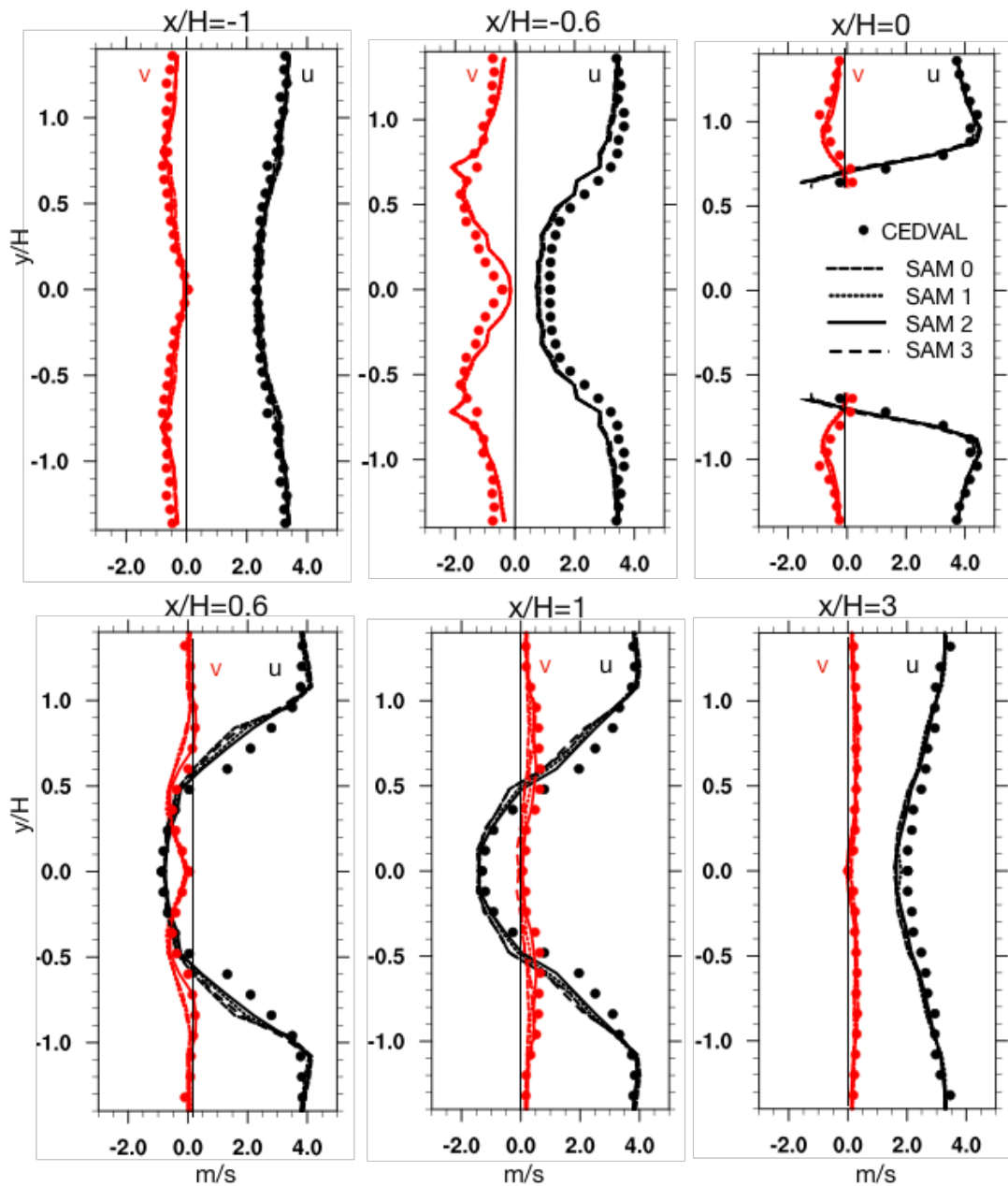
674

675

676

677

**Figure 3.** Vertical profiles of wind components at  $y/H=0$ . The results from SAM are shown by the lines for different number of iterations, from 0 to 3, as indicated in the top-right panel legend. Circles present the CEDVAL data; black and red colors represent the horizontal (u) and vertical (w) wind components, respectively.



678

679

680

681

682

683

684

**Figure 4.** Horizontal profiles of wind components at  $z/H=0.28$ . The results from SAM are shown by the lines for different number of iterations, from 0 to 3, as indicated in the top-right panel legend. Circles present the CEDVAL data; black and red colors represent the horizontal wind components of (u) and (w) wind components, respectively.

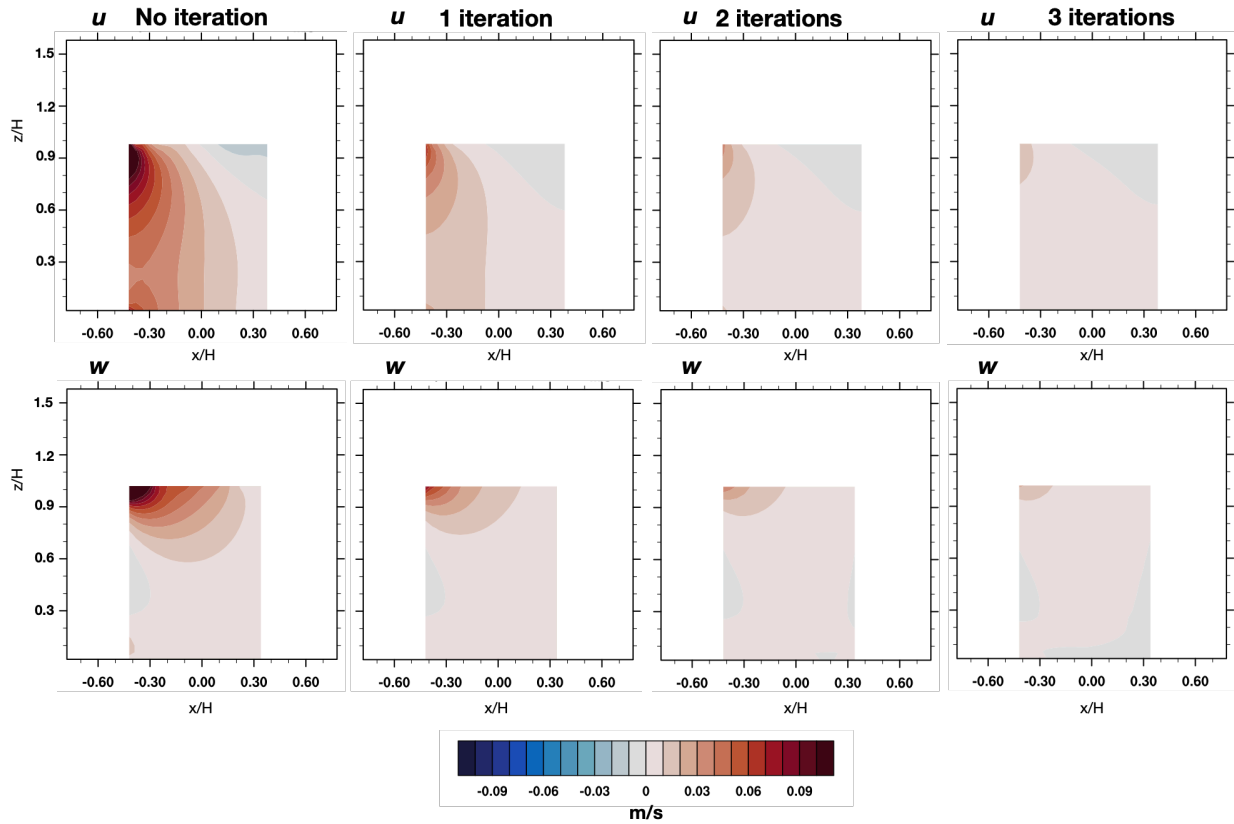


**Figure 5.** Residual horizontal  $u$  (top) and vertical  $w$  (bottom) velocities inside the building at  $y/H=0$  for no additional iteration (left), and several additional iterations over the steps (5)-(8) of the QSBM as indicated above the columns.

685  
686  
687  
688  
689  
690

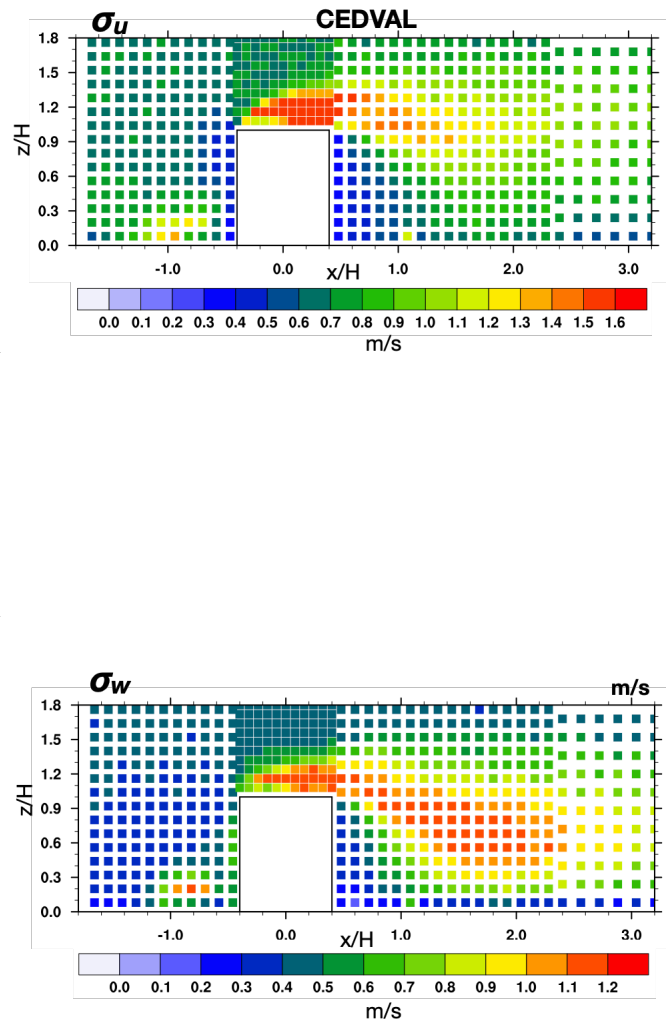
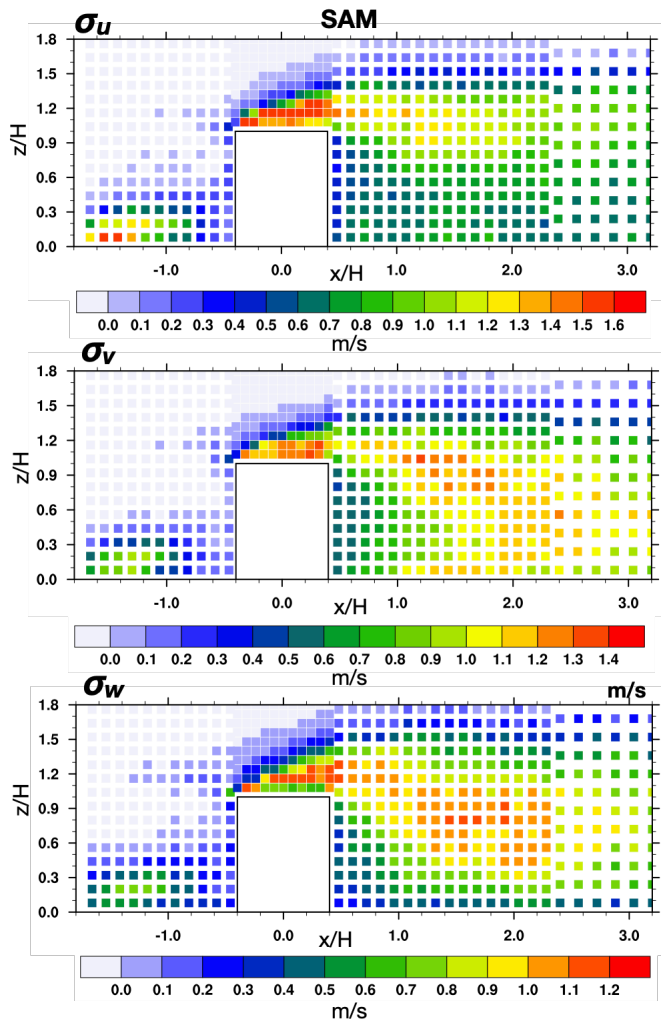


**Figure 6.** Turbulent intensity for different wind components at  $y/H=0$  for SAM (left panels) and CEDVAL observations (right panels). No observations are available for  $v$  component. The measurement density is indicated by the discrete points plotted (i.e., no interpolation is used).

691  
692

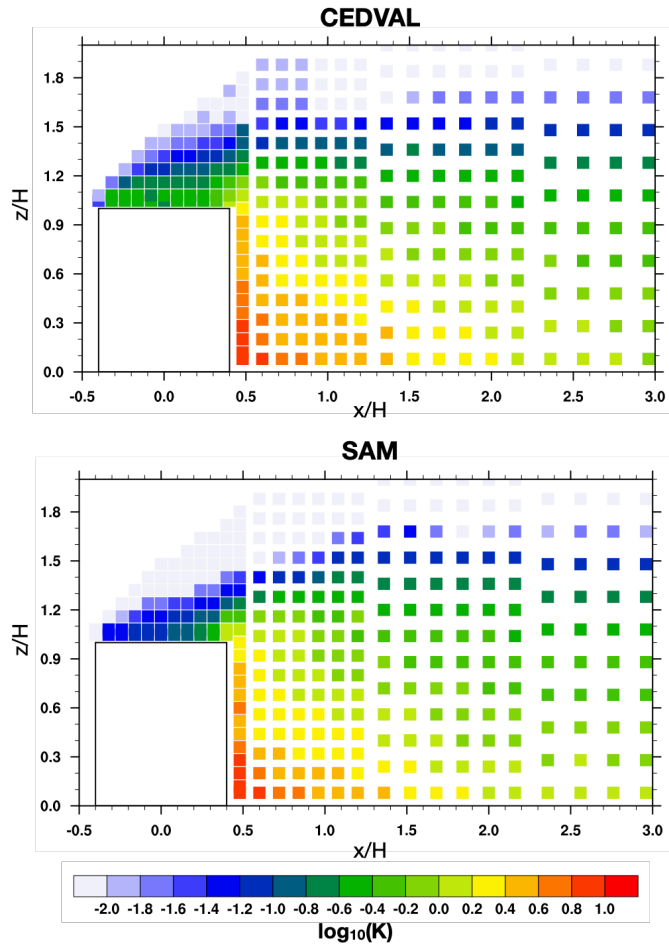


**Figure 7.** The dimensionless gas tracer concentration in the vertical symmetry plane  $y/H=0$  for CEDVAL A1-5 observations (top) and SAM (bottom). The measurement density is indicated by the discrete points plotted (i.e., no interpolation is used).

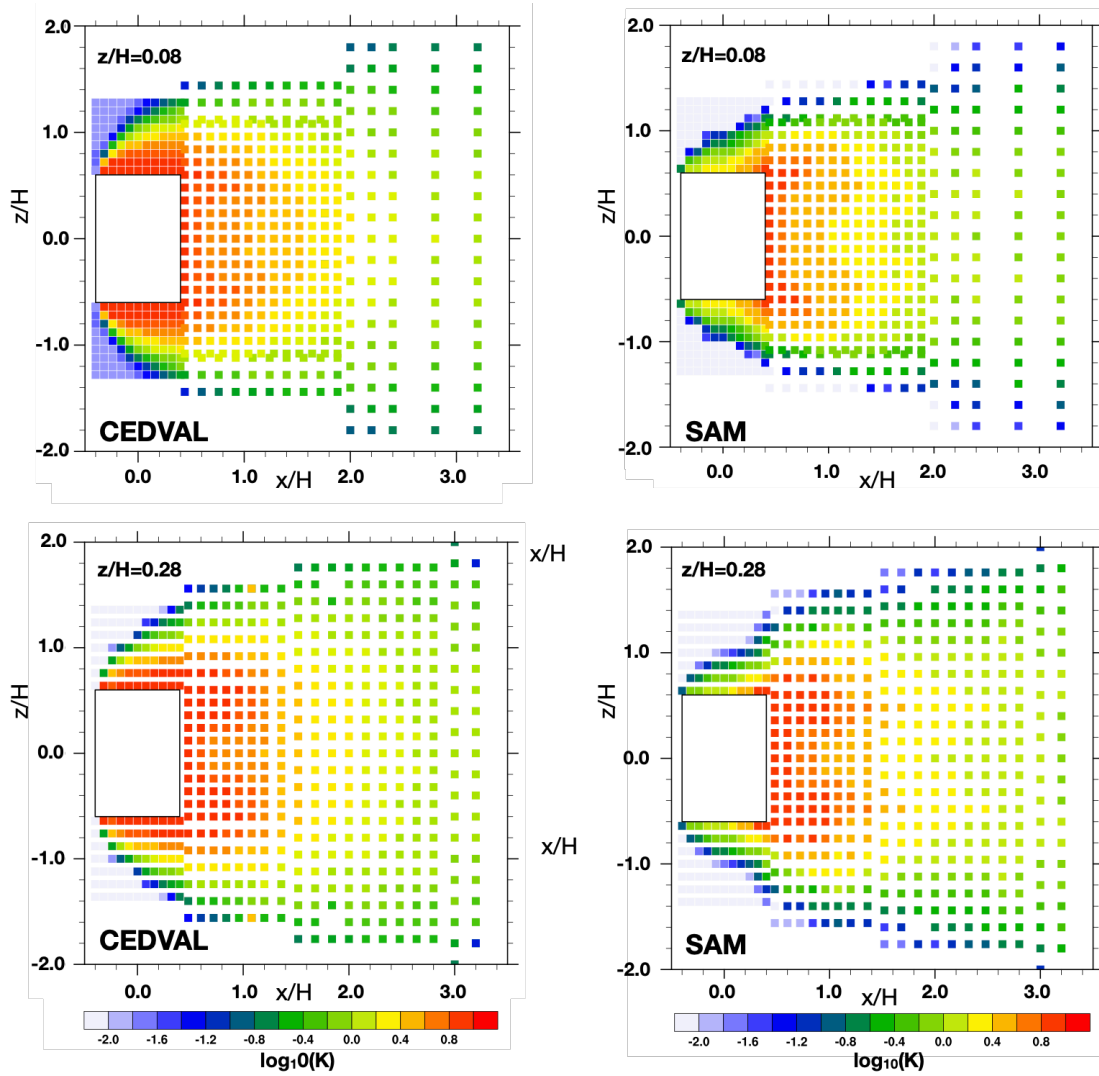


**Figure 8.** The dimensionless gas tracer concentration in the horizontal planes  $z/H=0.08$  (top) and  $z/H=0.28$  (bottom) for CEDVAL A1-5 observations (left) and SAM (right). The measurement density is indicated by the discrete points plotted (i.e., no interpolation is used).

694  
695  
696  
697  
698  
699  
700  
701  
702  
703  
704

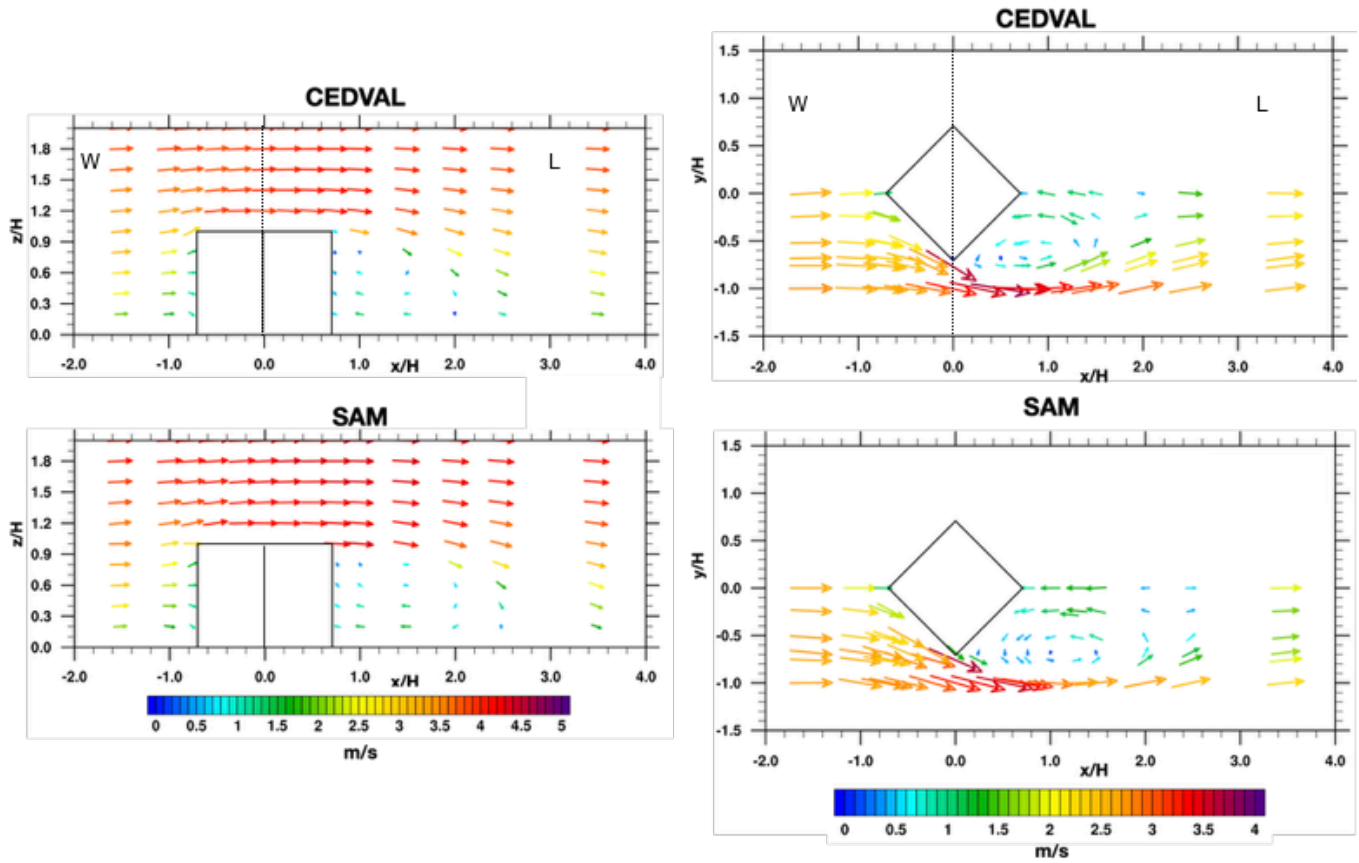


**Figure 9.** Vertical  $x$ - $z$  cross-section at  $y/H = 0$  (left panels) and horizontal  $x$ - $y$  cross-section of wind at  $z/H = 0.4$  (right panels) for CEDVAL A1-6 experiment (top) and SAM simulation (bottom). The coordinates are normalized by the building's height  $H$ . The dashed lines in the top plot indicate the boundaries of the key zones used for statistical comparison: W – windward in front of the building; L – leeward vortex and wake zone.

705  
706  
707  
708  
709  
710  
711  
712  
713  
714  
715  
716  
717

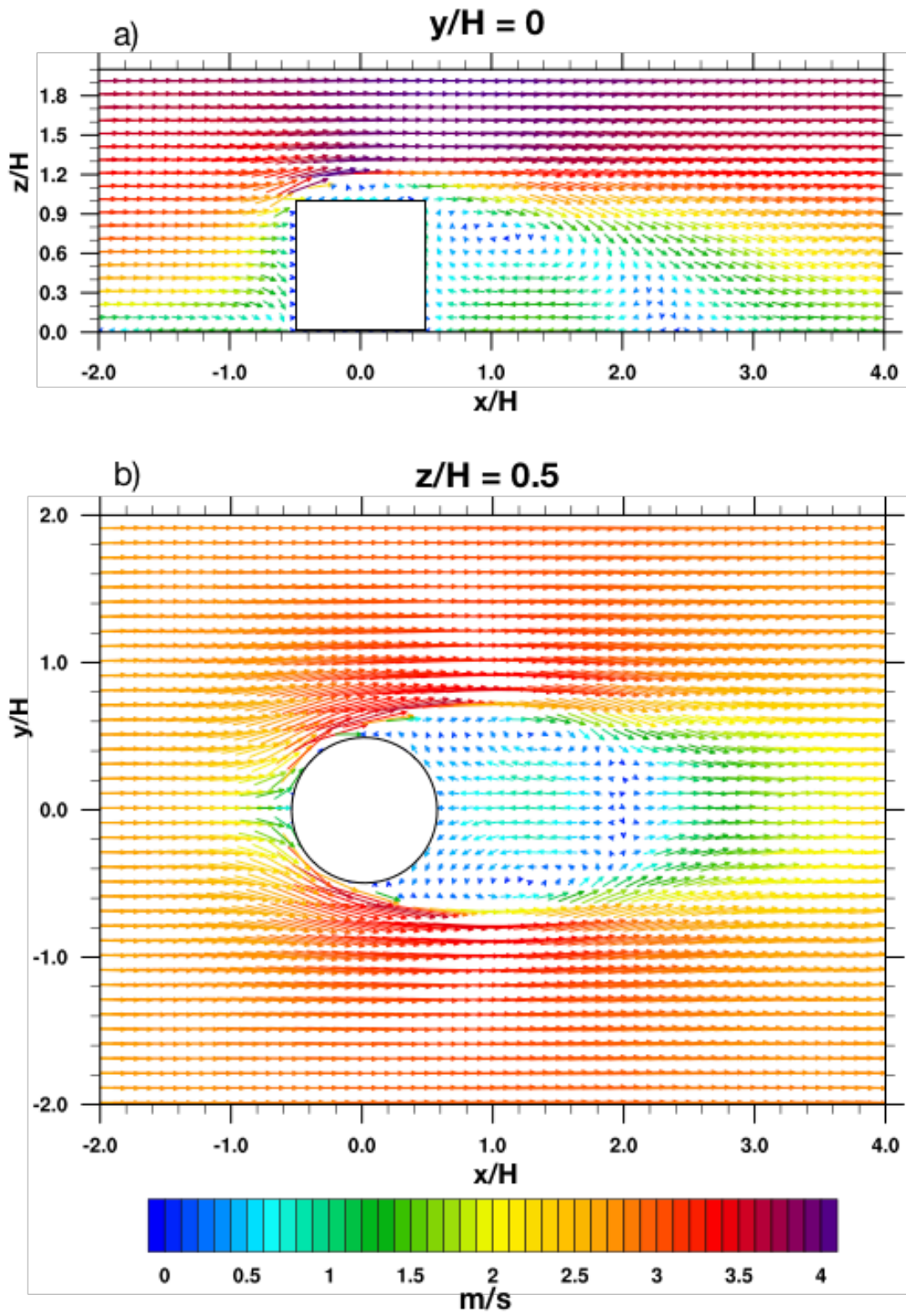
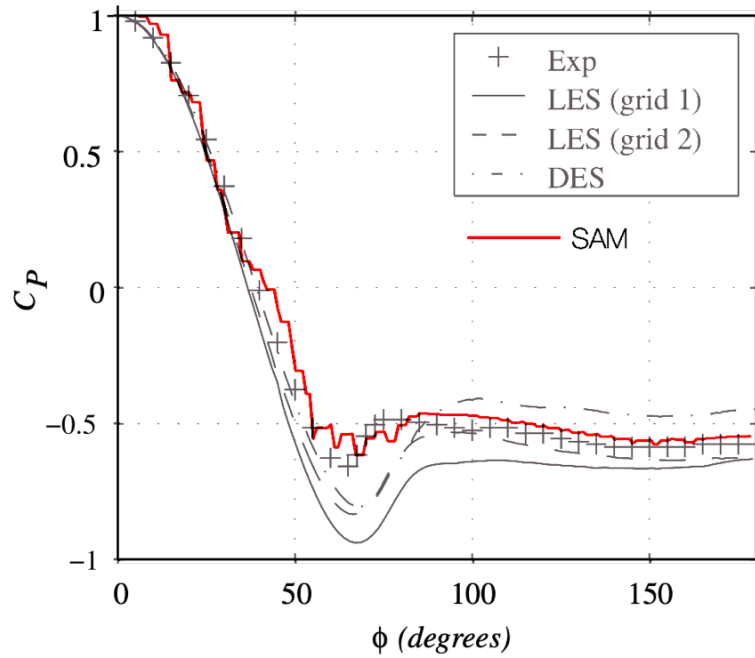


**Figure 10.** (a) Vertical cross-section at  $y/H=0$  and (b) horizontal cross-section at  $z/H=0.5$  of time-averaged wind for simulated flow around a cylinder with aspect ratio of one. The coordinates are normalized by height of the cylinder. The wind magnitude is shown by vector length as well as by its color.

721  
722  
723  
724  
725  
726  
727  
728  
729  
730



731  
732

**Figure 11.** Pressure coefficient  $C_P$  near the surface of the cylinder as a function of cutting angle around it at  $z/H=0.5$ . Results from SAM (red line) are superimposed on Fig. 7 from Pattenden et al (2007), which shows their modeling (LES, DES) and experimental results (Exp).

1                   **The Quasi-Solid Box Method for Simulating Wind Around Obstacles in**  
2                   **the System for Atmospheric Modeling**

3  
4                   Marat F. Khairoutdinov<sup>1</sup>, Andrew M. Vogelmann<sup>2</sup>, and Katia Lamer<sup>2</sup>

5  
6                   <sup>1</sup> School of Marine and Atmospheric Sciences, Stony Brook University, Stony Brook, New York, USA

7                   <sup>2</sup> Brookhaven National Laboratory, Upton, New York, USA

8  
9  
10   Key points:

- 11       • A simple modification to the anelastic equations in the System for Atmospheric Modeling  
12       enables explicit resolution of the flow around buildings.
- 13       • The accuracy of the methodology is demonstrated using single-building wind tunnel data.

14  
15   **Abstract**

16  
17       A novel method to represent the flow around obstacles such as buildings is developed and  
18   incorporated into the System for Atmospheric Modeling (SAM). The Quasi-Solid Box Method (QSBM)  
19   introduces a simple modification to the anelastic equations that forces the flow to stagnate within the  
20   obstacle's boundaries. The performance of the modified SAM is evaluated using CEDVAL (Compilation  
21   of Experimental Data for Validation of Microscale Dispersion Models) wind tunnel measurements of the  
22   wind and tracer dispersion around a single rectangular building. All major flow features are well  
23   simulated, such as the arch vortex leeside of the building, height of the flow separation point in front of  
24   the building, "separation bubbles" over the rooftop and on building sides, and leeside return flow towards  
25   the building. The dispersion of the tracer released at the building base is also simulated quite reasonably.  
26   To demonstrate the ability of the method in more general cases when buildings boundaries do not conform  
27   to the grid-cell boundaries, we report results for successful simulation of a flow around a cubic building  
28   rotated by 45° relative to the flow, and around a building in the form of a cylinder of aspect ratio of one.  
29   The QSBM has virtually no additional computational cost and can be implemented in any anelastic model.

30  
Corresponding author: Marat Khairoutdinov, marat.khairoutdinov@stonybrook.edu

31 **Plain Language Summary**

32

33 A novel method to simulate the wind and turbulence around obstacles, such as buildings, has been  
34 developed for use in a computer model that was previously used only to study turbulence and clouds over  
35 flat Earth surface. The method, called the Quasi-Solid Box Method, forces the simulated flow to stop in  
36 the model grid-cells that are inside an obstacle. The accuracy of the method is tested using cases of a flow  
37 past an idealized single rectangular building, a cubic building rotated by 45°, and a building in the form  
38 of a cylinder. The simulations are compared with wind tunnel observations around a small model building  
39 and to results from other models. The modeled gas tracer dispersion around the building also agrees quite  
40 well observations. We also report results for successful simulation of a flow around a cubic building  
41 rotated by 45° relative to the flow, and around a building in the form of a cylinder of aspect ratio of one.  
42 The main appeal of the new method is its simplicity that requires very minor modifications to the model  
43 code. The improved model can be used for detailed studies of the impact of climate change on urban  
44 environments.

45

46

47 **1. Introduction**

48

49 Predicting how climate change will impact the Earth’s climate system is a longstanding goal that  
50 has motivated the development of an array of global climate models. Historically, climate models have  
51 been focused on predicting how climate change will impact natural environments. As 55% of the world’s  
52 population now lives in cities (Profiroiu et al., 2020), there has been growing interest in understanding  
53 how climate change will impact human stress as well and also how urban features themselves affect the  
54 stress level. Urban environments are visibly complex with their mix of land use and array of surface types.  
55 The high-level of heterogeneity and small scale of urban elements further motivates the general trend  
56 towards developing higher-resolution models.

57 The System for Atmospheric Modeling (SAM; Khairoutdinov & Randall, 2003) is a  
58 computationally efficient model that has been widely used within the community to study atmospheric  
59 processes. Its computational efficiency comes from the use of the anelastic approximation to the

60 momentum equations and is fully scalable to run as a cloud-resolving model at kilometer resolutions down  
61 to only a few meters as a large-eddy simulation model. This high degree of scalability presents an  
62 opportunity to simulate climate impacts on urban microclimates down to street-resolved resolutions. Such  
63 simulations, however, require an efficient way to represent heterogeneous urban landscapes and,  
64 particularly, how they affect wind flow and transport within streets and around buildings. Winds are  
65 chosen as a starting point as they act to ventilate heat, moisture and gas tracers and disperse of airborne  
66 contaminants. This paper provides a computationally efficient framework to make simulations building-  
67 aware in anelastic models such as SAM.

68         There are various methods for incorporating the impact of obstacles on wind flow in atmospheric  
69 models. The terrain-following coordinate transformation method (Gal-Chen & Somerville, 1975) has been  
70 used in many atmospheric models to incorporate the terrain. Unfortunately, its application may encounter  
71 some problems; for example, pressure gradient forces along a curved coordinate can lead to spurious flows  
72 at high model resolutions near steep terrain (e.g., Fortunato and Paptista, 1996). More importantly though,  
73 its application in SAM would require abandoning the use of the non-iterative bidirectional Fast Fourier  
74 Transform (FFT) solver for Poisson equation for pressure (which would include cross-derivatives),  
75 resulting in reduced computational efficiency and the need for development of an iterative elliptic equation  
76 solver.

77         There are other methods to modeling a flow past obstacles, such as buildings, in the computational  
78 fluid dynamics (CFD) community. One is to generate a curvilinear structured or unstructured grid that  
79 conforms to the obstacle's outer boundaries (e.g., Hanna, 2006; Blocken, 2018). However, in this case,  
80 modeling a different set of buildings would require generation of an entirely different grid. Local grid  
81 refinement would also be typically used to better resolve the flow near an obstacle's boundaries, especially  
82 when a building has a complex shape with many sharp edges. Arguably, this is the most comprehensive  
83 approach, but it may be quite complicated and computationally expensive, with complex grid-generation  
84 techniques that minimize the skewness of the resultant grids. Another popular method is the Immersed  
85 Boundary Method (IBM). In the IBM, the grid does not necessarily conform to the obstacle's outer  
86 boundaries and can be, for example, a regular Cartesian grid. For this method, an accurate algorithm is  
87 also needed to determine exactly where the buildings' surfaces lie relative to the specified grid. Then,  
88 carefully crafted forcing terms are added to the model momentum equations to force the velocity to be

89 tangential to the projected surface of an obstacle (e.g., Iaccarino and Verzicco, 2003; Mittal & Iaccarino,  
90 2005). The advantage of the IBM is that the obstacle’s actual boundaries are captured as opposed to being  
91 truncated by the grid cell boundaries. Also, for moving obstacles, the grid does not have to change; only  
92 the boundary’s current position should be recomputed. The IBM has been used in atmospheric models to  
93 simulate flow over terrain (Lundquist et al., 2010), blunt objects, and buildings in the atmospheric  
94 boundary layer (e.g., Lundquist et al., 2010; Kumar and Tiwari, 2021). However, implementing the IBM  
95 in SAM would not only require abandoning the FFT solver for the pressure equation, but it would also  
96 involve performing careful interpolation of the velocity flow at each time step, and possibly local grid  
97 refinement, to improve accuracy. As a result, it would lead to considerable code modifications and may  
98 generate complications arising from the requirement that, in the anelastic equations used in SAM, the  
99 predicted momentum field must be non-divergent at the end of each time step.

100 In one of the variants of the IBM, sometimes called the “body-force method”, the flow is not forced  
101 to be tangential to the projected building surface but, rather, fictitious nudging terms are used to force the  
102 velocity of the flow inside the obstacle to stagnate over a time horizon comparable to the model time step  
103 (Chen & Leach, 2007; Smolarkiewicz et al., 2007; Korycki et al. 2016; Muñoz-Esparza et al., 2020). An  
104 advantage of the body-force method is that it can also be used to represent porous obstacles such as trees.  
105 The nudging time scale is usually chosen to be inversely proportional to the wind velocity; as such, in  
106 high wind conditions the model time step may have to become very small for stability of the time  
107 integration scheme, which results in increase computational expense.

108 In this study, we propose and test a variant of the “body-force method”, which we call the Quasi-  
109 Solid Box Method (QSBM). In principle, the QSBM can be applied to any anelastic or Boussinesq model.  
110 The method allows one to halt the flow almost completely inside a chosen group of cells comprising an  
111 obstacle, and it does not require any explicit nudging terms. Also, the method does not impact the  
112 integration time step, which remains bounded by the usual Courant–Friedrichs–Lewy (CFL) stability  
113 constraint which is based on the resolved velocity already in SAM. The practical advantage of the QSBM

114 is that it is very simple and requires very minor code changes; further, the FFT solver for the pressure  
115 equation does not require any modifications, thus preserving SAM's computational efficiency.

116         The main drawback of the QSBM is that it requires approximation of an obstacle's shape by using  
117 only whole grid cells; this may create staircase-like boundaries for otherwise smooth boundaries that do  
118 not conform to the model grid, which may create additional noise and turbulence. However, this potential,  
119 additional turbulence is not considered to be of concern for the intended application of this method in  
120 SAM which is to simulate the flow and tracer transport around a city that is already immersed in a highly  
121 turbulent atmospheric boundary layer. This is fortunate as a rather coarse resolution is available to  
122 represent the many individual buildings within the city without incurring an enormous computational cost.  
123 We note that the real buildings, unlike many idealized models of buildings used in wind-tunnel  
124 experiments, have many irregular surface features—such as window cavities, balconies, architectural add-  
125 ons—that usually are not well represented by computer models anyway, but which can also produce  
126 turbulence. In addition, the turbulent flow in the boundary layer around real buildings itself is not very  
127 well resolved at small scales, even when large-eddy simulation (LES) is used. Within the context of the  
128 flow around the whole city, it is not clear how important all these details of the buildings (inherently  
129 unresolved by any LES) actually are to generating additional turbulence, which would require additional  
130 research in the future.

131         This paper is organized as follows. Details regarding the implementation of the QSBM in SAM  
132 are described in Section 2. A demonstration of the performance of the QSBM is provided in Section 3  
133 where we compare an LES of the flow past a single rectangular building against wind-tunnel  
134 measurements. In this case, the building orientation is such that its boundaries ideally conform to the  
135 Cartesian grid's cell boundaries. Therefore, in Section 4, we also demonstrate the generality of the method  
136 through results for two additional simulations of the flow around obstacles with the boundaries that do not  
137 conform to the grid cell boundaries. The first case is the flow around a cubic building rotated 45° to the  
138 direction of the flow, and the second case is the flow around a building in the form of a circular cylinder.  
139 A summary of the results is provided in Section 5.

140

## 141 **2. The Quasi-Solid Box Method (QSBM)**

142

143 Prognostic velocities in anelastic models, like SAM, cannot be simply set to zero at the boundaries  
144 of cells inside obstacle at the end of each time step because it would violate the non-divergence equation  
145 and lead to noise and numerical instability; thus, we design a method to produce a similar result. Like in  
146 the body-force method, the proposed QSBM adds a simple Newtonian damping nudging term to the  
147 momentum equations:

148

$$\frac{\partial \mathbf{u}}{\partial t} = \mathbf{A} - \nabla \pi - \frac{\mathbf{u}}{\tau} \quad (1)$$

149

150 where  $\mathbf{u}$  is the velocity vector,  $\nabla \pi$  is the pressure gradient,  $\tau$  denotes a damping time scale, and  $\mathbf{A}$  denotes  
151 all other terms like advection, diffusion, Coriolis force, etc. One can see that the damping term forces the  
152 wind to decelerate and eventually stop over some time. For the Arakawa-C grid, this damping term is  
153 activated for all the velocity components at the sides of each cell located inside an obstacle; otherwise, no  
154 damping is applied.

155 To reproduce the effect of wind stopping abruptly at the face of an obstacle,  $\tau$  in (1) should be  
156 infinitesimally small. However, since SAM uses the explicit third-order Adams-Bashforth (AB3) scheme  
157 for time integration, the minimum allowed value for  $\tau$  is approximately two time-steps for a non-  
158 oscillatory solution (Duran, 1991); otherwise, the computations would be unstable or oscillatory. As  
159 damping to near zero would take at least a time interval of  $3 \tau$ , or about six time-steps, it is obvious that  
160 such damping would be of no practical use—the flow would easily penetrate deep into the obstacle before  
161 stagnating; or, in the case of a relatively small obstacle, even go right through it. Therefore, a much smaller  
162 damping time scale is required.

163 One way to avoid numerical instabilities while introducing damping terms to the velocity  
 164 acceleration terms is to use an implicit scheme as follows. First, the provisional wind field  $\mathbf{u}^*$  is obtained  
 165 using only the  $\mathbf{A}$  terms:

$$166 \quad \mathbf{u}^* = \mathbf{u}^n + \Delta t^n (a\mathbf{A}^{n-1} + b\mathbf{A}^{n-1} + c\mathbf{A}^{n-2}) \quad (2)$$

167 where  $a$ ,  $b$ , and  $c$  are AB3 coefficients that depend on the current time step  $\Delta t^n$  and past time steps  
 168  $\Delta t^{n-1}$  and  $\Delta t^{n-2}$ . Next, the implicit correction to the provisional solution is made to include the  
 169 damping term:

$$170 \quad \mathbf{u}^{**} = \mathbf{u}^* - \mathbf{u}^{**} \frac{\Delta t^n}{\tau} \quad (3)$$

171 noting here that the implicit approximation (3) is computationally stable for any value of  $\tau$ . Equation (3)  
 172 can be rewritten as

$$173 \quad \mathbf{u}^{**} = \mathbf{u}^* \frac{1}{1 + \frac{\Delta t^n}{\tau}} \quad (4)$$

174 This form makes it easy to see that in the limiting case where flow comes to a complete stop at the obstacle  
 175 boundary for  $\tau = 0$ , or *instantaneous* relaxation, the factor  $\frac{1}{1 + \frac{\Delta t^n}{\tau}}$  becomes zero too. Given this, it is  
 176 sufficient to require that the *corrected provisional velocity*  $\mathbf{u}^{**}$  be zero at all sides of the cells inside an  
 177 *obstacle*, i.e.,

$$178 \quad \mathbf{u}^{**} = 0 \quad \text{at all sides of cells inside an obstacle} \quad (5)$$

179 and there is no need to specify a value for  $\tau$ . Note, however, that representing the flow through porous  
 180 obstacles such as bushes and trees would require setting some explicit value to the relaxation time-scale  
 181  $\tau$  in (4). The final solution can then be obtained by performing the pressure-correction step

$$182 \quad \mathbf{u}^{n+1} = \mathbf{u}^{**} - \Delta t^n (a\nabla\pi^n + b\nabla\pi^{n-1} + c\nabla\pi^{n-2}) \quad (6)$$

183 where  $\pi^n$  is unknown and should be obtained from the solution of an elliptic equation following

$$184 \quad \nabla(\rho\nabla\pi^n) = \frac{1}{a\Delta t^n} \nabla \cdot \rho\mathbf{u}^{**} - \frac{b}{a} \nabla(\rho\nabla\pi^{n-1}) - \frac{c}{a} \nabla(\rho\nabla\pi^{n-2}) \quad (7)$$

185 which is derived using the mass continuity constraint on the final velocity field:

$$\nabla \cdot \rho \mathbf{u}^{n+1} = 0 \quad (8)$$

It is important to realize that requiring  $\mathbf{u}^{**}$  to be zero at all sides of the cells inside an obstacle does not automatically mean that the final velocity  $\mathbf{u}^{n+1}$ , obtained from the pressure correction (6)-(7), will also be exactly zero; this is due to the inherently non-local nature of the elliptic equation for which the solution at a particular point depends simultaneously on the solution for the whole grid. However, as will be shown in Section 3d, the velocity field inside the obstacle is very small compared to the velocities right outside it. This outcome is explained by the fact that the pressure correction to the provisional velocity  $\mathbf{u}^{**}$ , to enforce continuity at each time step, is generally small. This is because the velocity change over a single time step is generally small, causing only a small divergence of the provisional momentum field to develop, which is precisely non-divergent at the beginning of each time step. The suppression of velocity inside obstacles can be further improved by iterating steps (5)-(7), which would make the final velocity  $\mathbf{u}^{n+1}$  after the pressure correction be a new provisional velocity  $\mathbf{u}^*$  to obtain the total solution (note that the solutions for pressure at each additional iteration should be added to the solution at previous iteration). Each additional iteration would add some additional computational expense to solving the elliptical equation (7). Obviously, the additional iterations only improve the solution inside the obstacles or near them and do not have any effect on the solution when obstacles are not present. As will be demonstrated in this study, the existence of small residual velocities does not seem to affect the simulated flow outside the obstacle in any significant manner; therefore, the iterations may not be even needed in most cases. This notion is consistent with results by Chen & Leach (2007), who compared an accurate solid-building approach to a simplified approach in which buildings are modeled by nudging the velocity to zero. A rather significant resultant nonzero residual flow occurred inside the buildings, but they also found a relatively small effect of such approximation on the external flow. Note that in some more traditional and accurate IBM approaches applied to anelastic or incompressible models, an expensive elliptic equation also needs to be solved at least twice on each time step (e.g., Zhang and Zheng, 2007).

### 3. Simulation of the flow around rectangular building

212

213 To test the performance of the QSBM in simulating the flow around solid obstacles, we performed  
214 two LES simulations for the case of a single rectangular building and compared it to the observational  
215 dataset from the Compilation of Experimental Data for Validation of Microscale Dispersion Models  
216 (CEDVAL; <https://mi-pub.cen.uni-hamburg.de/index.php?id=433>). We use reference cases from A1-1,  
217 which have been previously used for evaluation of other numerical models (e.g., Diehl et al., 2007; Gorlé  
218 et al., 2010; Trini Castelli & Reisin, 2010; Parente et al., 2011; Zhang et al., 2016). Specifically, we will  
219 use A1-1 to evaluate the velocity field and A1-5 to evaluate the dispersion of a gas tracer.

220

### 221 *a) Case setup*

222

223 The A1-1 setup aims to present a building that is 20 m long in the downwind direction, 30 m wide  
224 in the crosswind direction, and reaches a height ( $H$ ) of 25 m. In the wind tunnel, this setup is approximated  
225 with elements that are about 200 times smaller, counting on the fact that similarity arguments at very large  
226 Reynolds numbers allow one to extrapolate the results to the target building size. The scaling factor of  
227 200 is suggested by the CEDVAL and has been used by other models. In SAM, the building is represented  
228 on a Cartesian grid with a uniform grid-spacing of 1 m and domain size of 400 x 200 x 100 m in downwind  
229 ( $x$ ), crosswind ( $y$ ), and the vertical ( $z$ ) directions, respectively. The horizontal dimensions of the domain  
230 closely reproduce the wind tunnel's dimensions multiplied by the scale factor of 200 while the domain  
231 top corresponds to only about half of the height of the actual wind tunnel. The reduced extent of the  
232 domain top, relative to the wind tunnel, was deemed acceptable as preliminary tests have shown that the  
233 flow barely changes at the height of the domain top. In the SAM simulation, the building center is located  
234 in the domain center at coordinates  $x = 0$ ,  $y = 0$  with its base at  $z = 0$ .

235

236 The horizontal inflow wind velocity used in the simulations is specified using a simple power-law  
237 profile  $u(z) = U_{ref}(z/H_{ref})^a$ , which is suggested by the CEDVAL and closely approximates the  
238 observed inlet profile. The factor  $a$  is set to 0.21 for both the A1-1 and A1-5 simulations. Then for A1-1  
and A1-5, respectively, the reference height,  $H_{ref}$ , is set to 100 m and 125 m, and the reference windspeed,

239  $U_{ref}$ , is set to 6.0 and 5.85 m/s. In both simulations, the inflow wind is aligned along the x direction. Since  
240 SAM uses a periodic domain in that direction, strong nudging of the wind profile is applied in the first  
241 10% of the domain length (in the x direction) to maintain a close match to the specified inflow profile.  
242 Solid walls are placed at the four other sides of the domain to mimic the wind tunnel's walls. One caveat  
243 to mention is that the incoming flow in the CEDVAL experiments has been found to be somewhat  
244 turbulent with about a 20-30% turbulent intensity that is quite anisotropic, with horizontal turbulence  
245 having higher intensity than vertical turbulence. However, in our experiments we assume that the  
246 incoming flow is not turbulent as there is no clear way to initiate the required turbulence characteristics,  
247 which may have been caused by the particular construction of the wind-tunnel inlet. In terms of  
248 atmospheric stability, the temperature stratification is set to neutral to represent the wind-tunnel  
249 conditions.

250 The advection scheme used for all scalars is the fully three-dimensional monotonic and positive  
251 scheme MPDATA (Smolarkiewicz, 2006). The advection scheme for momentum is the second-order,  
252 centered-differences-in-flux form with conservation of kinetic energy. The surface everywhere is free-slip  
253 for simplicity, as at high Reynolds numbers (like in this case) the drag by the building surface does not  
254 have a large effect on the flow (it may affect the incoming profile near the surface, but we specify it). It  
255 might be important to use subgrid-scale (SGS) turbulent viscosity. However, for this case we tried both  
256 the Smagorinsky and 1.5-order closure for the SGS turbulence, based on prognostic SGS kinetic energy,  
257 and found little difference between the results.

258 To see the effect of additional iterations of the QSBM on the results and on the residual flow inside  
259 the building, three additional experiments were performed with one, two and three iterations. As will be  
260 discussed further, the number of iterations had small effect on overall results. Therefore, rather arbitrarily,  
261 most of the result will be presented using the simulation with two additional iterations.

262 Both simulations were run for 3900 s with a 0.05 s timestep. The first 900 steps are discarded as  
263 spin-up, so only the last 3000 s (i.e., 50-minutes) of each run are used for time averaging of the results.  
264 The averaging period is 750 times longer than characteristic time scale given by  $H/U_{ref}$  and, therefore,

265 more than sufficient to obtain a statistically steady solution. Even though this may seem to be a very long  
266 integration, for the wind-tunnel model of the building, which is 200 times smaller, this simulation time  
267 would correspond to about 15 seconds in the wind tunnel. Also note that because SAM is a parallel and  
268 efficient model, each simulation took only about an hour on a supercomputer using 200 cores; therefore,  
269 by any measure, it cannot be considered a “computationally expensive” simulation.

270

271 *b) Gas tracer release*

272

273 The QSBM allows for small “leaks” of momentum and kinetic energy into the obstacles which may  
274 not be problematic for most applications but may become a problem for advection of conserved scalars.  
275 Thus, simulating the dispersion of gas tracer releases requires one additional code modification: setting  
276 the flux of scalars through the obstacles’ boundaries to zero. In CEDVAL, the gas tracer is continuously  
277 released from four elongated openings at the bottom of the leeward wall of the building (representing four  
278 entrances to a parking garage) with a flow rate of 3 m/s; that is, they are not simple point sources. In SAM,  
279 these sources are simply modeled by four 3-grid-point continuous sources (i.e., 3 m) in the y direction  
280 right near the wall. Due to the constraint imposed on mass conservation in the incompressible model, it  
281 would be difficult to specify an additional flow of air, as in the actual gas tracer sources in CEDVAL. The  
282 absence of this additional flow may be responsible for some of the biases in the results. The CEDVAL  
283 dataset reports normalized gas tracer concentrations  $K$ , defined it as  $K = C \times U_{ref} \times H^2 / Q_s$ , where  $C$  is  
284 actual concentration and  $Q_s$  is total specified gas tracer release rate. This normalization process eliminates  
285 the need to produce a precise match between observed and simulated release rates such that an arbitrary  
286 release rate can be used in the model.

287

288 *c) Time-average flow*

289

290 The A1-1 dataset contains wind measurements for two planes, vertical at  $y/H=0$  (i.e., vertically  
291 through the center of the building) and horizontal at  $z/H=0.28$  (i.e., horizontally at 7 m above the base of  
292 the building). We begin by performing a qualitative evaluation of the main flow features in the planes as  
293 a whole, and then we offer a more qualitative evaluation in specific columns of the model.

294 Beginning with the vertical plane, Figure 1 illustrates the 50-min averaged flow streamlines  
295 (combined  $u$ ,  $w$  components) color coded by the wind speed in the wind tunnel (top panel) and in the  
296 simulation (bottom panel). Overall, the simulation captures well the main observed features of the flow  
297 around the building in this plane. In front of the building below the rooftop level, the flow separates into  
298 the so-called horseshoe vortex, where below  $\sim 2/3$  of the building height the flow dives towards the surface  
299 while above that height the flow rides upward and over the building rooftop. Both the observations and  
300 model show a rotation vortex upwind of the building face near the surface. That said, we note that the  
301 rotation center of the simulated vortex is farther away from the building than in observations. Over the  
302 rooftop of the building, a “separation bubble” develops, which is well reproduced by the model. In the  
303 building’s wake, a large leeside vortex is present, which, on this  $x$ - $z$  cross-section, is a visible part of a so-  
304 called “arch vortex” developing behind the building. The flow reverses direction in the low part of the  
305 leeside vortex, resulting in converging flow towards the building and rising flow along the leeside wall  
306 towards the rooftop. The position of the center of rotation of the leeside vortex is captured by the model  
307 quite well, albeit the simulated position is a bit higher than observed. Also, the simulated vortex extends  
308 as far as  $x/H = 1.9$  (47 m) in the simulation compared to  $x/H = 1.7$  (42 m) in the observations. We note  
309 that other models also have tended to overextend the leeside vortex in this CEDVAL case (e.g., Górlé et  
310 al., 2010; Trini Castelli & Reisin, 2010; Parente et al., 2011; Zhang et al., 2016).

311 Table 1 summarizes the comparison with the CEDVAL observations for the whole  $y/H=0$  plane  
312 as well as for three key zones shown in Figure 1, the windward zone (W), leeside zone (L), and the zone  
313 above the rooftop (R). Here we follow the methodology by Zhang et al. (2016). The mean relative error  
314 ( $RE$ ) of the wind velocity for the whole plane is 2.0% with an  $RMSE$  of 0.42 m/s; the overall spatial  
315 correlation with observations  $R = 0.97$ . As expected, the biggest challenge for the model is the leeside

316 flow, where the  $RE$  is the largest, 18.6%, and  $R = 0.91$ . The windward  $RE$  is rather small, 1.6% but,  
317 because of the error in the center position of the horseshoe vortex, the correlation is only 0.87. The flow  
318 over the rooftop is simulated the best, with  $RE = 0.7\%$  and  $R=0.98$ .

319 Moving on to the horizontal plane, Figure 2 illustrates the 50-min averaged flow streamlines  
320 (combined  $u$ ,  $v$  components) color coded by the wind speed in the wind tunnel (top panel) and in the  
321 simulation (bottom panel). Again, the main characteristics of the flow in that plane are well reproduced  
322 by the model. Those include the “separation bubbles” at the building’s sides that consist of two  
323 counterrotating vortices and the position of rotation centers at the leeside of the building. This pair of  
324 vortices at the leeside is also a part of the arch vortex. The acceleration of the flow around the building  
325 corners is well reproduced not only qualitatively, but also quantitatively.

326 Table 2 summarizes the statistics of the flow for the whole  $z/H=0.28$  plane as well as separately  
327 for three key zones shown in Figure 2, the windward zone (W), the zone across the lateral walls (S), and  
328 leeside zone (L). For the whole plane,  $RE = 9.4\%$  and  $R=0.91$ . The largest  $RE = 16.1\%$  is found in the  
329 front of the building with  $R=0.93$ . The overall leeside flow is reproduced better, with  $RE= 10.2\%$  and  
330  $R=0.92$ . Despite the fact that the model performs better in the zone across the lateral walls in terms of the  
331 mean wind with  $RE = 7.1\%$ , the spatial correlation of the wind velocity is only  $R = 0.86$ . Overall, our  
332 statistical results summarized by Tables 1 and 2 are quite close to the results presented by Zhang et al.  
333 (2016).

334 Figures 3 and 4 offer another way of evaluating the simulated flow in the same planes as the  
335 previous figures. In addition, these figures present results obtained for using different number of iterations  
336 of the QSBM whereas Figures 1 and 2 only show results using 2 iterations.

337 Beginning with the vertical plane, Figure 3 shows vertical profiles of the 50-min mean horizontal  
338 (along the  $x$  axis;  $u$ ) and vertical ( $w$ ) velocities at various distances from the building center along the  $x$   
339 axis at  $y/H = 0$  (i.e., along the direction of the wind passing through the center of windward and leeward  
340 building faces). As mentioned above, the main inconsistency with the observations is that the horseshoe  
341 vortex near the surface is relatively farther upstream from the building, as evident by the velocity profiles

342 at  $x/H = -1$ . Closer to the windward wall ( $x/H = -0.6$ ), the magnitude of both downward and upward vertical  
343 velocities and the position of the stagnation point ( $w = 0$ ) are reproduced quite well, although  $w$  near the  
344 rooftop level is overestimated by about 1 m/s. Both profiles above the rooftop at the building's center  
345 ( $x/H=0$ ) are reproduced very well. The profiles through the leeside vortex ( $x/H = 0.6$  and  $x/H = 1$ ) also  
346 show good agreement with the observations. One can clearly see the reverse return flow towards the  
347 building throughout most of the building height. The profile of the mean wind in the building's wake at  
348  $x/H = 3$ , which is relatively far away from the flow reconnection point, is also well reproduced.

349 Moving on to the horizontal plane, Figure 4 shows horizontal profiles of  $u$  and  $v$  at various  
350 distances from the building center along the  $x$  axis at  $z/H = 0.28$ . Overall, the profiles are reproduced quite  
351 well by the model. There is a slight underestimation of the incoming velocity in front of the building at  
352  $x/H=-0.6$ . Also, there are two “kinks” in the corresponding  $v$  profile in front of the building corners at the  
353 distance of  $\pm 0.7$  from the center line, which can be explained by some noise generated by the second-order  
354 advection scheme for momentum because of the sharp corners of the building. The acceleration of the  
355 flow and the flow towards the building near its side walls at  $x/H=0$  is in good agreement with observations.  
356 In the leeside, at  $x/H=0.6$  and  $x/H=1.0$ , the magnitude of the return flow towards the building is reproduced  
357 very well, although the downwind velocity outside of the return flow is clearly underestimated. The  
358 profiles of the reconnected flow at  $x/H=3.0$  is also well reproduced.

359

#### 360 *d) Residual flow inside the building*

361

362 The results shown in Figures 3 and 4 indicate that the number of iterations used in the QSBM have  
363 only a minor impact on the mean flow. For completeness, we explore their impact on the residual flow  
364 inside the building. Figure 5 shows the 50-min mean horizontal (along the  $x$  axis;  $u$ ) and vertical ( $w$ )  
365 velocities or “residual velocities” in the vertical plane  $y/H = 0$  (i.e., along the direction of the wind passing  
366 through the center of windward and leeward building faces) for simulations relying on various numbers  
367 of iterations in the QSBM. When no iterations are performed, the maximum residual velocity inside the

368 building is about 0.1 m/s at the upper inflow corner. The largest standard deviation of the residual velocity  
369 is smaller than 0.005 m/s (not shown). Considering that the inflow wind is several meters-per-second, it  
370 is fair to say these residual velocities are already quite small. Each iteration further reduces the residual  
371 velocity by about a factor of two; so after two and three iterations, the maximum residual velocities in the  
372 plane decrease to about 0.02 and 0.01 m/s, respectively. In terms of computational expense, the bi-  
373 directional-FFT pressure solver takes about 20% of running time in the particular parallel model  
374 configuration running on 200 CPUs, so each additional iteration adds about 20% to the expense.

375

376 *e) Turbulence*

377

378 So far, we have presented time averaged results. It is also important to see the ability of the model  
379 to simulate the turbulence associated with the flow around a building. As was mentioned above, the  
380 incoming flow in the simulation is not turbulent, but the incoming flow in the wind-tunnel experiment  
381 already has some turbulence, especially in the  $u$ -component. There is no simple way to initialize the  
382 anisotropic turbulence in the model to mimic the turbulence at the inlet of the wind tunnel. The turbulent  
383 kinetic energy of the incoming flow would contribute some additional turbulence behind the building, and  
384 this factor is absent in the simulation. However, most of turbulence is generated by the building itself;  
385 therefore, with the aforementioned caveat in mind, we will still compare the turbulent intensities produced  
386 by the model against the observations.

387 Figure 6 compares the turbulent intensity, or the standard deviation of turbulent wind velocity  
388 fluctuations, individually for each of the wind components in the vertical symmetry plane  $y/H = 0$ .  
389 Unfortunately, only turbulent intensities for the  $u$  and  $w$  components of the wind are reported in that plane  
390 by the CEDVAL A1-1 dataset. The region with maximum turbulence is just above the building rooftop in  
391 both the simulations and observations. On the leeward side, the turbulence is relatively weak immediately  
392 behind the building within the distance approximately equal to the building's height, as in observations.  
393 The highest levels of turbulent intensity of the  $u$  component are generally above the building's rooftop

394 height as observed. On the contrary, the maximum intensity of the  $w$ -component is generally below the  
395 rooftop height mostly above the upper half of the building. Overall, the spatial structure of the turbulent  
396 regions behind in the wake of the building is well reproduced by the model.

397

398 *f) Gas tracer transport*

399

400 Figure 7 shows normalized gas tracer concentration in the vertical plane at  $y/H=0$ . The greatest  
401 concentrations are found near the ground close to the leeside wall, where the sources are. In the simulation,  
402 the gas tracer concentration reaches a maximum of 56.3 normalized units vs the 66.7 normalized units in  
403 the wind tunnel. The gas tracer is transported by the leeside vortex up along the leeward wall towards the  
404 rooftop, where it gets swept into the “separation bubble” above the rooftop. Overall, the model seems to  
405 reproduce the observed distribution of concentration rather well, especially throughout the leeside vortex,  
406 but tends to underestimate concentration above the rooftop.

407 Figure 8 shows normalized gas tracer concentration in horizontal planes at  $z/H = 0.08$  (2 m) and  
408  $z/H = 0.28$  (7 m). Overall, the horizontal distribution of gas tracer concentration at the leeside is reproduced  
409 quite satisfactory in both horizontal planes. The main model biases are within the “separation bubbles”  
410 along the side walls of the building, like the one over the rooftop, where concentration is also  
411 underestimated. Nevertheless, the gas tracer seems to penetrate all the way to the front corners of the  
412 building, like in observations. The apparent difficulty that the model has with the cavities along the side  
413 walls and over the rooftop can be attributed to the flow being rather unresolved there, as the thickness of  
414 the “bubbles” (see Figures 1 and 2) are only several grid cells. Also, as mentioned before, the sources of  
415 gas tracers in the wind-tunnel experiment are not point sources but, rather, are jets ejecting gas tracer with  
416 the speed of 3 m/s from four elongated openings in the leeward building’s wall. It is not clear how to  
417 mimic such dynamic sources of gas tracers in SAM.

418

#### 419 **4. Simulations of obstacles not aligned with the grid**

420

421 In the previous section, we reported the results of flow around an idealized rectangular building  
422 when the boundaries are perfectly aligned with the grid cells' boundaries which, arguably, is an ideal  
423 situation for testing our method. However, an important question remains as to how universal the proposed  
424 method is when applied to obstacles with boundaries that are not aligned with the numerical grid. To  
425 answer this question, we apply the QSBM method to two other cases. In the first case, we simulate the  
426 flow around a building in a shape of a cube rotated  $45^\circ$  relative to the flow and also to the grid; i.e., with  
427 its corner facing the incoming flow. In the second case, we consider flow around a building in the form of  
428 a circular cylinder with a height/diameter ratio of one. In each case, an obstacle is represented by a  
429 population of whole grid cells that fit inside its actual geometric boundaries.

430

431 *a) A cubic building rotated  $45^\circ$*

432

433 This test is based on the CEDVAL A1-6 case of a cube rotated  $45^\circ$  relative to the direction of the  
434 incoming flow. In the dataset, the size scaling factor of 200 is also suggested, so the cubic building has  
435  $H=25$  m size for all dimensions. The incoming flow profile is the same as in A1-1 case. The model grid  
436 and duration of the run are also identical to our simulation of the A1-1 case. Figure 9 compares model to  
437 observations, showing the wind vectors at the  $y/H=0$  symmetry plane and horizontal cross-section at the  
438  $z/H=0.4$  height. Note that, unlike the A1-1 case, the measurements of the wind in A1-6 case were relatively  
439 sparse. In the figure, all the available data are plotted, with model results shown at the same locations as  
440 the measurements. One can see that in the case of rotated cube, there is a clear horse-shoe vortex does not  
441 develop upstream from the building as was the case in A1-1. There is also virtually no acceleration of the  
442 flow above the building and no indication of the separation bubble developing over the roof. The bulk of  
443 the flow seems to prefer to go around the building's side corners rather over the top of the building. The  
444 model seems to capture this behavior rather well, both qualitatively and quantitatively. In the leeside of  
445 the building, the arch-vortex also develops, with a leeside vortex and associated reverse flow towards the  
446 building clearly visible in the vertical cross-section. The leeside extent of the flow seems to be somewhat

447 overestimated in the simulation, as in the A1-1 case, but it is difficult to quantify that difference due to  
448 the sparsity of observations. Similar to the A1-1 case, there is a pair of vortices behind the building (only  
449 one of them is actually shown), clearly visible in the horizontal cross-section. The model seems to shift  
450 the center of rotation further downstream than in observations, probably because of the rather rough  
451 representation of the building walls in this case when the grid is not aligned with the building surfaces.

452 Tables 3 and 4 present statistics of comparisons with the CEDVAL observations for  $y/H=0$  and  
453  $z/H=0.4$  planes, respectively, for windward zone (W) and leeside zone (L) shown in Fig. 9 as well as for  
454 all observations for a given plane. For the vertical  $y/H=0$  plane, the  $RE$  of the wind velocity is 7.6% with  
455 an  $RMSE$  of 0.42 m/s and  $R = 0.96$ . The biggest challenge for the model is before is the leeside flow,  
456 where the  $RE$  is the largest, 9.3%, and  $R = 0.94$ . The windward  $RE$  is also relatively large, 6.2%, but the  
457 correlation is very high 0.99. The flow over the rooftop is simulated the best, with  $RE = 0.7\%$  and  $R=0.98$ .  
458 For the horizontal  $z/H=0.28$  plane as the whole,  $RE = 6.1\%$  and  $R=0.91$ . The largest  $RE = 13.5\%$  is found  
459 again in the leeside zone with  $R=0.89$ , while the windward zone is simulated much better with  $RE = 4.2\%$   
460 and  $R=0.94$ . Overall, we may conclude that the flow in this case of rotated cubic building is simulated  
461 reasonably well.

462

#### 463 *b) A flow around a circular cylinder*

464

465 To further investigate the ability of our method to simulate the flow around obstacles that have  
466 boundaries not aligned with the Cartesian grid, we simulate the flow around a circular cylindrical building  
467 with the aspect ratio (ratio of height to diameter) of one. We use the setup from an LES study by Kumar  
468 and Tiwari (2021; further KT21), which, in turn, is based on the experimental and LES results reported  
469 by Pattenden et al (2007; further P07). The latter used a structured grid conformal to the cylinder shape,  
470 while the former used the conventional IBM on a Cartesian grid. In KT21, the incoming wind profile was  
471 obtained first by a separate LES simulation of a neutral surface layer over a flat surface with a given  
472 roughness length  $z_o$ . It was found that the resultant profile is very close to a log-law profile

473  $u(z) = \frac{u_*}{k} \ln \frac{z}{z_o}$ , where  $u_*=0.29$  m/s,  $z_o=0.046$  m, and  $k$  is von Karman constant. In KT21, the height of  
474 the cylinder is 4 m. We scaled up the size of the cylinder by a factor of 10 to  $H=40$  m, which would be a  
475 more reasonable size for a building. To maintain the self-similarity of the flow, a factor of 10 increase was  
476 also applied to the roughness length in the specified log-law wind profile, yielding  $z_o = 0.46$  m. The grid  
477 spacing was also increased to 1 m from the 0.1 m in KT21, to preserve the relative grid resolution of the  
478 cylinder. The numerical domain is chosen to be the same in the horizontal directions as in the previous  
479 runs, but the domain is twice as tall because the building is also taller than before. The time step and run  
480 duration were the same as in the previous runs.

481 Figure 10 illustrates the overall structure of the time-averaged flow around the cylinder showing  
482 velocity vectors in the vertical plane through the center of the cylinder as well as in the horizontal plane  
483 at cylinder's mid-height. Overall, all the features that we saw in the case of rectangular building are  
484 present, namely: a horse-shoe vortex in front of the cylinder, an arch-vortex in the leeside with the return  
485 flow towards the cylinder in its wake with a pair of counterrotating vortexes, and the separation "bubble"  
486 over its top. The flow features are consistent with the results presented by KT21 (see their Figs 5 and 6).  
487 However, there are some clear differences. Similar to the simulation of the rectangular building, the horse-  
488 shoe vortex is overextended upstream with the position of separation point near the surface at  $x/H = -2$   
489 compared to the observed  $x/H = -1$  given in P07. This is probably due to our use of free-slip conditions  
490 and insufficient vertical resolution near the surface. Note that the position of the separation point is also  
491 overextended in KT21 ( $x/H = -1.5$ ) and LES results by P07 ( $x/H = -1.45$ ). The height of the stagnation  
492 point, where the separation of the incoming flow into upward and downward branches occurs at the  
493 upstream surface of the cylinder, is at  $z/H = 0.7$ , which is close to  $z/H = 0.65$  reported by KT21. The  
494 surface position of the flow reattachment point of the leeside vortex is also overextended at about  $x/H =$   
495  $2.2$ , compared to the observed  $x/H = 1.6$ . However, the KT21 and P07 studies also had difficulty  
496 reproducing this parameter, reporting  $x/H = 1.95$  and  $x/H = 2.1$ , respectively. On the top of the cylinder,  
497 the reattachment of the separated flow is at  $x/H = 0.35$ , same as in KT21 and close to  $x/H = 0.39$  in P07.

498 It is rather common when modeling the flow around blunt objects, such as a cylinder, to look at a  
 499 so-called pressure coefficient:  $C_p = (p - p_\infty) / \frac{1}{2} \rho V_\infty^2$ , where  $p$  is the pressure on the object's surface,  $\rho$  is  
 500 air density,  $p_\infty$  and  $V_\infty$  are the pressure and velocity upstream of the flow far from the object. In the case  
 501 of a cylinder, the pressure coefficient is measured along its surface at some fixed height as a function of  
 502 the angle  $\Phi$  in cylindrical coordinates relative to the cylinder's center, usually between  $\Phi = 0^\circ$  and  $\Phi =$   
 503  $180^\circ$  which is between upstream and downstream points of the cylinder's surface. Figure 11 compares  $C_p$   
 504 at  $z/H = 0.5$  to the modeling and experimental results presented by P07 superimposing our results on their  
 505 Fig. 7. One can see that overall, the distribution of pressure coefficient near the cylinder's surface is  
 506 captured rather well by SAM. Some apparent noisiness of the SAM results is associated with the rather  
 507 rough approximation of the curved cylinder surface by rectangular cells in our method. We can also use  
 508 the pressure coefficient to compute the drag coefficient  $C_D$ , which, in case of a cylinder, is computed as  
 509  $C_D = \int_0^\pi C_p \cos \Phi d\Phi$  (e.g., Bertin 2002). From our results, we obtain the drag coefficient to be 0.82, which  
 510 is close to the observed value of 0.79 reported by P07.

511

## 512 **5. Summary**

513

514 In this paper, we present a method for incorporating obstacles, such as buildings, into SAM. This  
 515 model is usually used to address climate-related questions but can be also employed as an LES model to  
 516 answer emerging urban microclimate questions. The method, which we call the Quasi-Solid Box Method  
 517 (QSBM), can be considered to be a subset of the immersed-boundary method (IBM), called the force-  
 518 body methods, that stagnate the flow everywhere inside an obstacle. Unlike some other force-body  
 519 methods that use fictitious damping or relaxation terms in the momentum equations, the QSBM avoids  
 520 them by explicitly setting the provisional velocity components to zero in the cells that are inside an  
 521 obstacle, right before applying the pressure-gradient terms to enforce non-divergence of the flow.

522 We tested the method using a case of a flow past an idealized single rectangular building in neutral  
 523 atmospheric conditions and compared the results to the CEDVAL wind-tunnel observations. Overall, the

524 model performance in this case can be considered satisfactory. All major flow features are well  
525 reproduced, such as the existence of an arch vortex in lee of the building, the horseshoe vortex and the  
526 height of the separation point of the inflow in front of the building, and the “separation bubbles” over the  
527 rooftop and on building sides. The model has a difficulty, though, reproducing the exact position of the  
528 center of rotation of the horseshoe vortex and tends to overestimate slightly the extent of the leeside vortex.  
529 On the other hand, the vertical wind structure of the flow above the rooftop and downstream from it is  
530 reproduced quite well, particularly the strength of the return flow towards the leeside wall. The highest  
531 levels of turbulence are simulated above the building rooftop, in accord with observations. A relatively  
532 calm zone, with relatively low levels of turbulence, is found behind the building within the distance  
533 approximately equal to the building’s height, also as in observations.

534         The QSBM allows a residual flow inside the obstacles that is very small compared to the magnitude  
535 of velocity in its vicinity; however, the residual velocities can be further reduced by iterating over the last  
536 steps that enforce zero velocity and non-divergence of the flow. The added expense is about 20% increase  
537 of running time per each additional iteration. In this study, each additional iteration would reduce the  
538 maximum magnitude of residual velocities inside the building by about a factor of two. However, overall,  
539 the use of iterations makes only a minor improvement over the simulation with no iterations. This  
540 conclusion might not be generalizable, so, ideally, sensitivity of the results to at least a single iteration  
541 should be tested when the method is employed to simulate other cases.

542         We additionally evaluate the ability of this method to handle the dispersion of gas tracers. The gas  
543 tracer dispersion also agrees rather well with observations, although some challenges remain in  
544 reproducing transport of gas tracer into the “separation bubbles”, not only over the rooftop, but also along  
545 its crosswind sides.

546         One of the drawbacks of the QSBM is that it requires approximation of any obstacle as a collection  
547 of whole grid cells that fit inside the obstacle’s actual geometric boundaries. This was not a problem in  
548 our simulation of a rectangular building as, in this case, the grid-cell boundaries conform to the building’s  
549 boundaries perfectly. However, in the case of a city, simulated buildings may not conform to the grid-cell

550 boundaries; so, as a result, they may have staircase-like walls. To evaluate the performance of the method  
551 in such cases, we presented the results of two additional simulations. The first is based on another  
552 CEDVAL case of the flow around a cubic building rotated by  $45^\circ$  to the direction of the incoming flow;  
553 the second case is for a cylindrical building with the aspect ratio of one, obtained from a different  
554 observational dataset and to which our results are compared to published results from two other LES  
555 models. Overall, the rotated building results compare rather well to the wind tunnel observations, both  
556 qualitatively and quantitatively. The biggest bias was in the exact position of the arch-vortex and some  
557 overextension of the leeside-vortex. In the case of the flow around the cylindrical building, all major  
558 observed features of such a flow have been fairly well represented by the model. Some notable biases are  
559 found, such as the position of a horse-shoe vortex and the extent of the leeside vortex. However, these  
560 biases are generally similar to those shown by other LES models for this case, which can be the indication  
561 of some fundamental difficulties in simulating such obstacles that are not necessarily SAM-specific.  
562 Despite the biases in the position of vortices, the angular distribution of a pressure coefficient around the  
563 cylinder and closely related aerodynamic drag coefficient have been well simulated by SAM when  
564 compared to actual measurements.

565 Overall, we find the results of the tests reported in this study to be quite encouraging. However,  
566 we caution that the QSMB should not be viewed as computationally inexpensive alternative to a more  
567 comprehensive and accurate traditional IBM. We implemented this method in SAM primarily to be able  
568 to simulate the turbulence and tracer transport around a city in the planetary boundary layer, when the  
569 buildings are relatively coarsely represented due to the computational cost. For such problems, the QSMB  
570 becomes a very attractive approach as its implementation requires very minor code modifications without  
571 affecting the computational efficiency of SAM.

572

573 **Acknowledgements.** This work was supported by the Brookhaven National Laboratory under its  
574 Laboratory Directed Research and Development (LDRD) Program, Project #20-002. This research used  
575 resources of the National Energy Research Scientific Computing Center; a DOE Office of Science User  
576 Facility supported by the Office of Science of the U.S. Department of Energy under Contract No. DE-

577 AC02-05CH11231. All model output used in this study is accessible through NCAR Campaign Storage  
578 via Globus.

579

580

581

## References

582

583 Bertin J.J. (2002). *Aerodynamics for Engineers*, 4<sup>th</sup> edition, Prentice Hall.

584 Blocken, B. (2018). LES over RANS in building simulation for outdoor and indoor applications: A  
585 foregone conclusion? *Building Simulation*, 11(5), 821–870.

586 Chan, S. T., & Leach, M. J. (2007). A validation of FEM3MP with Joint Urban 2003 data. *J. Appl. Meteor.  
587 and Clim.*, 12, 2127–2146.

588 Diehl, S.R., Burrows, D.A., Hendricks, E.A., & Keith, R. (2007). Urban dispersion modeling: Comparison  
589 with single-building measurements. *J. Appl. Meteor. Climatol.*, **46**, 2180–2191.

590 Duran, D. R. (1991). The Third-Order Adams-Bashforth Method: An Attractive Alternative to Leapfrog  
591 Time Differencing. *Mon. Wea. Rev.*, 119(3), 702-720.

592 Fortunato, A. B., and A. M. Baptista, 1996: Evaluation of horizontal gradients on sigma coordinate  
593 shallow water models. *Atmos. Ocean* 34, 489-514.

594 Gal-Chen, T., & Somerville, C.J. (1975). On the use of a coordinate transformation for the solution of the  
595 Navier–Stokes equations. *J. Comput. Phys.*, 17, 209–228.

596 Gorlé, C., van Beeck, J., & Rambaud, P. (2010). Dispersion in the Wake of a Rectangular Building:  
597 Validation of Two Reynolds-Averaged Navier–Stokes Modelling Approaches. *Boundary-Layer  
598 Meteorol.*, **137**, 115–133. <https://doi.org/10.1007/s10546-010-9521-0>

599 Hanna, S., and Coauthors, 2006: Detailed simulations of atmospheric flow and dispersion in downtown  
600 Manhattan: An application of five computational fluid dynamics models. *Bull. Amer. Meteor. Soc.*,  
601 87, 1713–1726.

602 Iaccarino, G., and R. Verzicco, (2003). Immersed boundary technique for turbulent flow simulations.  
603 *Appl. Mech. Rev.*, 56, 331–347.

604 Khairoutdinov, M. F., & Randall, D.A. (2003). Cloud-resolving modeling of the ARM summer 1997 IOP:  
605 Model formulation, results, uncertainties, and sensitivities. *J. Atmos. Sci.*, 60, 607-625.

606 Korycki, M; Loboeki, L, and Wyszogrodzki, A, 2016: Numerical simulation of stratified flow around a  
607 tall building of a complex shape. *Environ. Fluid Mech*, 16(6), 1143-1171.

608 Kumar P. and Tiwari, S. (2021): Effects of size ratio and inter-cylinder spacing on wake transition in flow  
609 past finite inline circular cylinders mounted on plane surface, *Physics of Fluids*, 33, 023602  
610 <https://doi.org/10.1063/5.0037712>

611 Lundquist, K. A., F. K. Chow, and J. K. Lundquist (2010): An immersed boundary method for the  
612 Weather Research and Forecasting Model. *Mon. Wea. Rev.*, 138, 796–817, [https://](https://doi.org/10.1175/2009MWR2990.1)  
613 [doi.org/10.1175/2009MWR2990.1](https://doi.org/10.1175/2009MWR2990.1).

614 Lundquist K.A., Chow F.K., Lundquist J.K. (2012) An immersed boundary method enabling large-eddy  
615 simulations of flow over complex terrain in the WRF model. *Mon Wea Rev* 140, 3936–3955.  
616 <https://doi.org/10.1175/MWR-D-11-00311.1>

617 Muñoz-Esparza, D., Sauer, J. A., Shin, H. H., Sharman, R., Kosović, B., Meech, S., et al. (2020).  
618 Inclusion of building-resolving capabilities into the FastEddy® GPU-LES model using an immersed  
619 body force method. *J. of Adv. in Model. Earth Sys.*, 12, e2020MS002141. [https://](https://doi.org/10.1029/2020MS002141)  
620 [doi.org/10.1029/2020MS002141](https://doi.org/10.1029/2020MS002141)

621 Mittal, R., & Iaccarino, G. (2005). Immersed Boundary Methods. *Ann. Rev. of Fluid Mech.*, 37, 239–261.

622 Parente, A., Górlé, C., van Beeck, J., & Benocci, C. (2011). Improved k-ε model and wall function  
623 formulation for the RANS simulation of ABL flows. *Journal of Wind Engineering and Industrial*  
624 *Aerodynamics*, 99, 267–278.

625 Pattenden, R. J., N. W. Bressloff, S. R. Turnock, and X. Zhang, (2007): Unsteady simulations of the flow  
626 around a short surface-mounted cylinder. *Int. J. Numer. Methods Fluids*, 53, 895–914.

627 Profiroiu, C. M., Bodislav, D. A., Burlacu, S., & Rădulescu, C. V. (2020). Challenges of Sustainable  
628 Urban Development in the Context of Population Growth. *European Journal of Sustainable*  
629 *Development*, 9, 3, 51-57. doi: 10.14207/ejsd.2020.v9n3p51

630 Smolarkiewicz, P.K. (2006). Multidimensional positive definite advection transport algorithm: an  
631 overview. *Int. J. Numer. Methods Fluids*, 50, 1123–1144.

632 Smolarkiewicz, P. K., Sharman, R., Weil, J., Perry, S. G., Heist, D., & Bowker, G. (2007). Building  
633 resolving large-eddy simulations and comparison with wind tunnel experiments. *Journal of*  
634 *Computational Physics*, 227(1), 633–653.

635 Trini Castelli, S., & Reisin, T.G. (2010). Evaluation of the atmospheric RAMS model in an obstacle  
636 resolving configuration. *Environ Fluid Mech.*, **10**, 555–576. [https://doi.org/10.1007/s10652-010-](https://doi.org/10.1007/s10652-010-9167-y)  
637 [9167-y](https://doi.org/10.1007/s10652-010-9167-y)

638 Zhang, N., Du, Y., & Miao, S. (2016). A microscale model for air pollutant dispersion simulation in urban  
639 areas: Presentation of the model and performance over a single building. *Adv. Atmos. Sci.*, **33**, 184–  
640 192. <https://doi.org/10.1007/s00376-015-5152-1>

641 Zhang, N., and Z.C. Zheng (2007): An improved direct-forcing immersed-boundary method for finite  
642 difference application. *J. Comp. Phys.*, 221, 2250-268.

643

644

645

**Tables**

646 **Table 1** Comparison of CEDVAL A1-1 observations and simulation for the whole plane  $y/H=0$  and for zones shown  
 647 in Figure 1 for mean ( $MN$ ), absolute error ( $E = MN_{sim}-MN_{obs}$ ), relative error ( $RE=|E/ MN_{obs}|$ ), root-mean-square  
 648 error (RMSE), and correlation coefficient ( $R$ ).

Zone	$MN_{obs}(m/s)$	$MN_{sim}(m/s)$	$E (m/s)$	$RE$	$RMSE (m/s)$	$R$
W - Windward	2.59	2.63	0.04	1.6%	0.60	0.87
L - Leeseide	1.41	1.14	-0.26	18.7%	0.47	0.91
R - Rooftop	4.58	4.61	0.03	0.7%	0.29	0.98
$y/H=0$	3.28	3.22	-0.06	2.0%	0.42	0.97

649

650 **Table 2** Comparison of CEDVAL A1-1 observations and simulation for the whole plane  $z/H=0.28$  and for the zones  
 651 shown in Figure 2 for mean ( $MN$ ), absolute error ( $E = MN_{sim}-MN_{obs}$ ), relative error ( $RE=|E/ MN_{obs}|$ ), root-mean-  
 652 square error (RMSE), and correlation coefficient ( $R$ ).

Zone	$MN_{obs}(m/s)$	$MN_{sim}(m/s)$	$E (m/s)$	$RE$	$RMSE (m/s)$	$R$
W - Windward	2.51	2.11	-0.40	16.1%	0.50	0.93
L - Leeseide	2.48	2.23	-0.25	10.2%	0.53	0.92
S - Sides	3.42	3.18	-0.24	7.1%	0.79	0.86
$z/H=0.28$	2.81	2.55	-0.26	9.4%	0.55	0.91

653

654 **Table 3** Comparison of CEDVAL A1-6 observations and simulation for the whole plane  $y/H=0$  and for the zones  
 655 shown in Figure 9 for mean ( $MN$ ), absolute error ( $E = MN_{sim}-MN_{obs}$ ), relative error ( $RE=|E/ MN_{obs}|$ ), root-mean-  
 656 square error (RMSE), and correlation coefficient ( $R$ ).

Zone	$MN_{obs}(m/s)$	$MN_{sim}(m/s)$	$E (m/s)$	$RE$	$RMSE (m/s)$	$R$
W - Windward	3.23	3.43	0.2	6.2%	0.23	0.99
L - Leeseide	2.98	3.25	0.27	9.3%	0.55	0.94
$y/H=0$	3.21	3.45	0.24	7.6%	0.42	0.96

657

658 **Table 4** Comparison of CEDVAL A1-6 observations and simulation for the whole plane  $z/H=0.4$  and for the zones  
 659 shown in Figure 9 for mean ( $MN$ ), absolute error ( $E = MN_{sim}-MN_{obs}$ ), relative error ( $RE=|E/ MN_{obs}|$ ), root-mean-  
 660 square error (RMSE), and correlation coefficient ( $R$ ).

Zone	$MN_{obs}(m/s)$	$MN_{sim}(m/s)$	$E (m/s)$	$RE$	$RMSE (m/s)$	$R$
W - Windward	2.42	2.52	0.1	4.2%	0.23	0.94
L - Leeseide	1.81	1.56	-0.24	13.5%	0.57	0.89
$z/H=0.4$	2.08	1.95	-0.13	6.1%	0.44	0.91

661

662

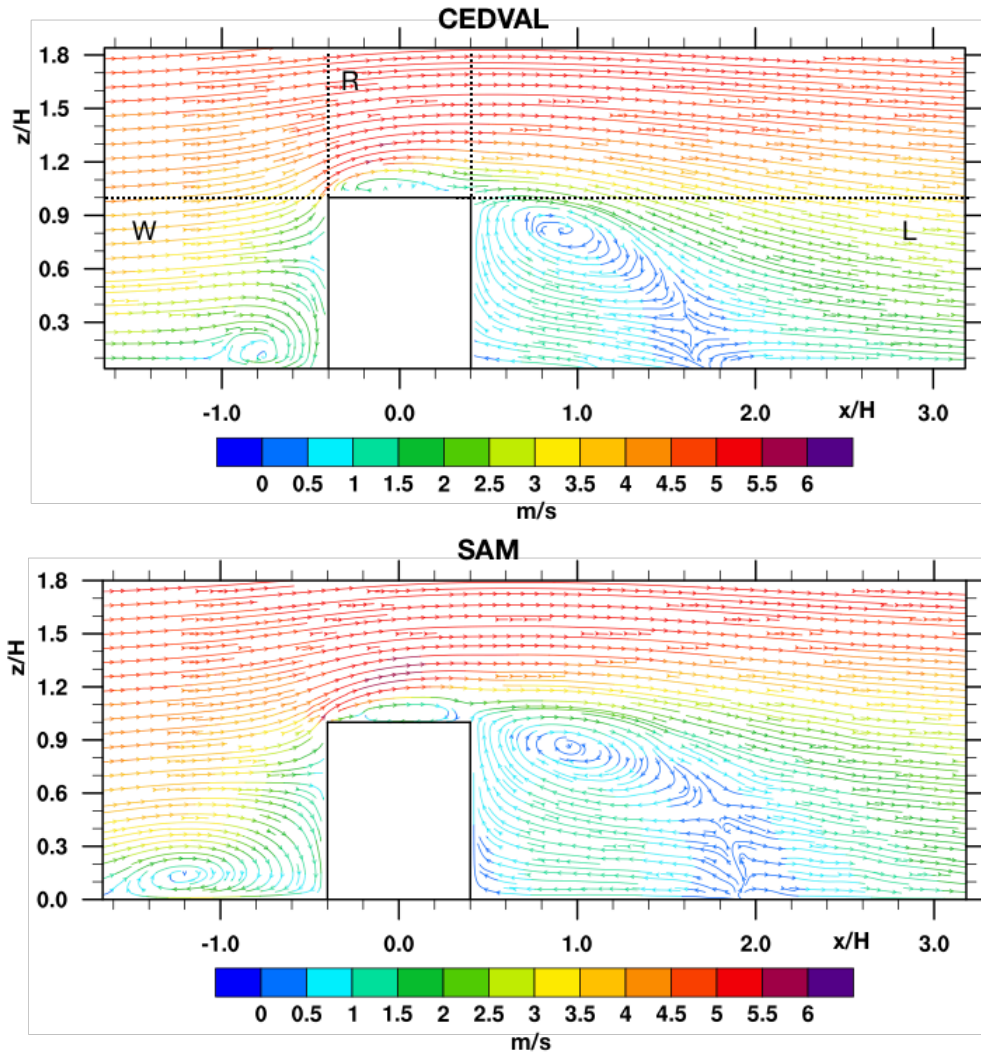
663

664

**Figures**

665

666

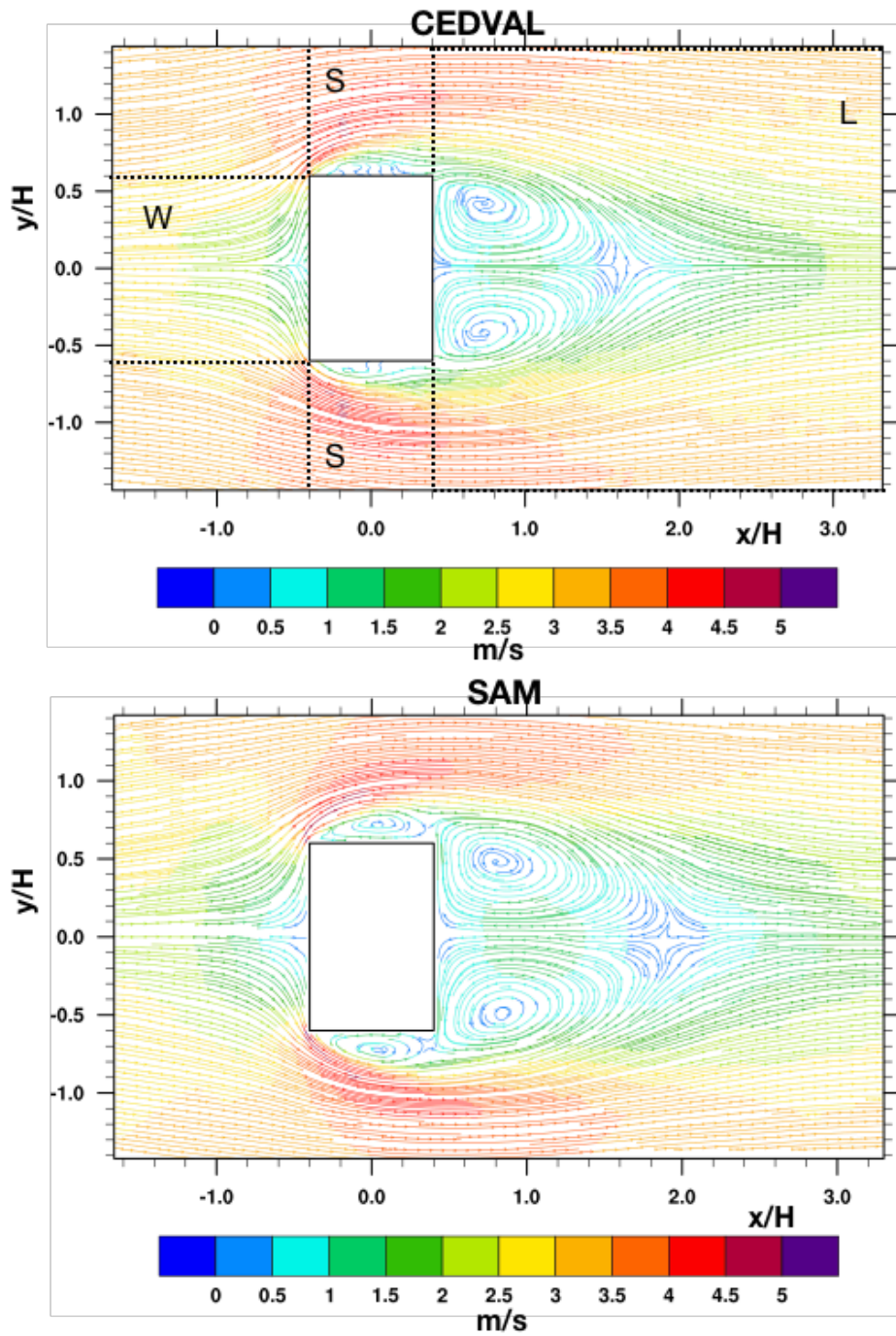


667

668

669

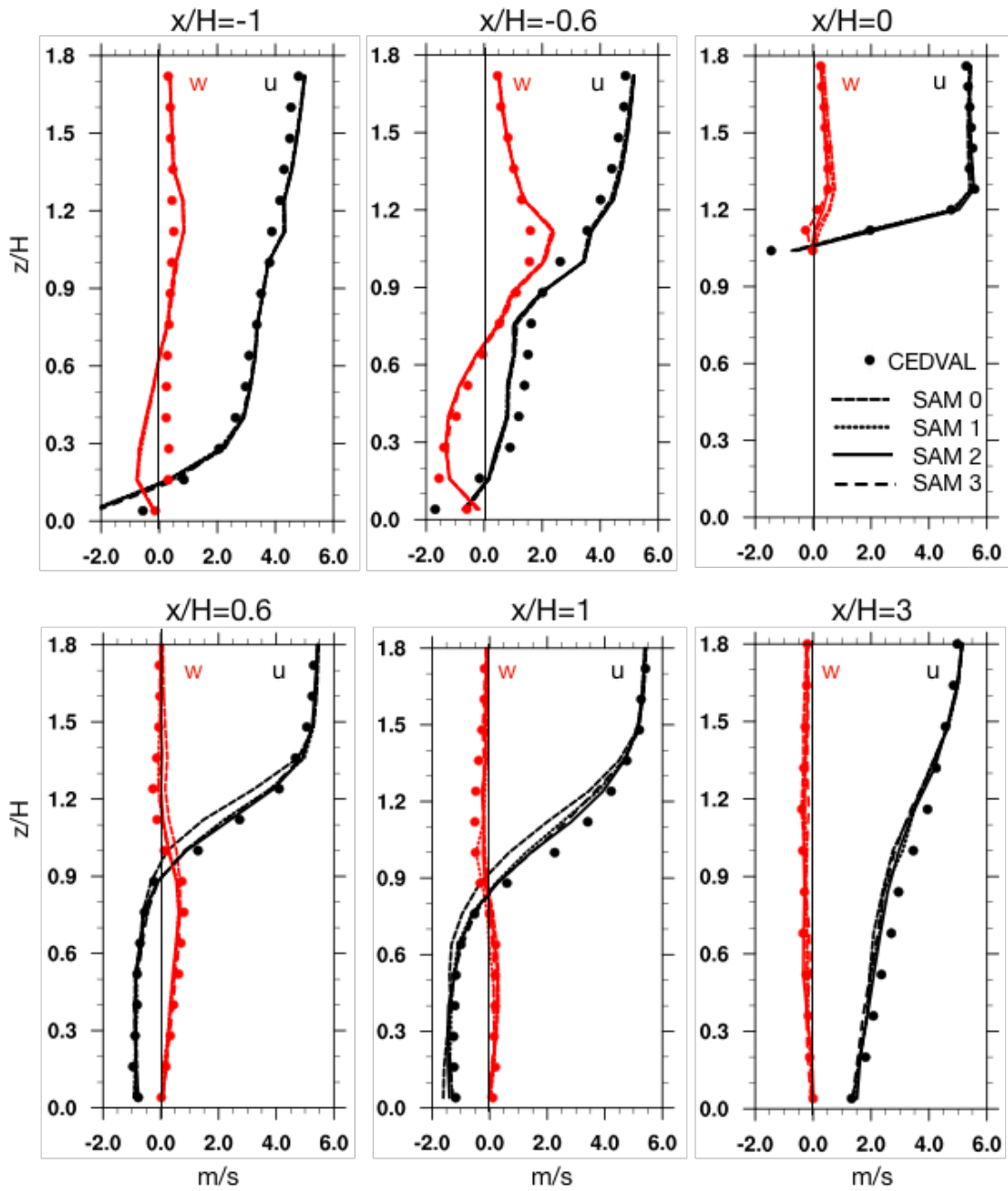
**Figure 1.** Vertical cross-section of wind at  $y/H = 0$  for CEDVAL observations (top) and SAM simulation (bottom). The coordinates are normalized by height of the building. The dashed lines in the top plot indicate the boundaries of the key zones used for statistical comparison: W – windward in front of the building; R – above the rooftop; L – leeside vortex and wake zone.



670

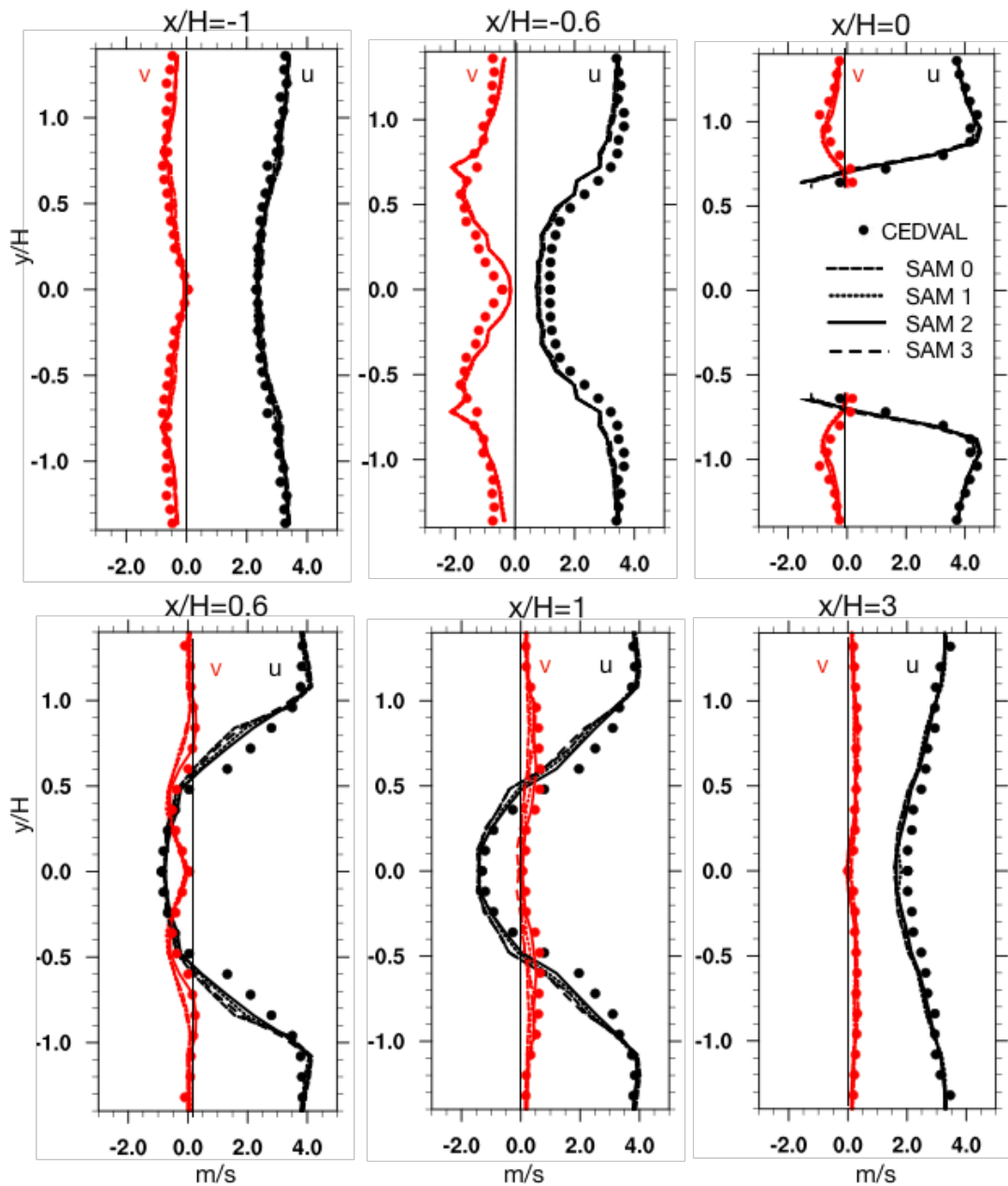
671

**Figure 2.** Horizontal cross-section of wind at  $z/H = 0.28$  for CEDVAL observations (top) and SAM simulation (bottom). The coordinates are normalized by height of the building. The dashed lines in the top plot indicate the boundaries of the key zones used for statistical comparison: W – windward in front of the building; S – across from lateral side walls; L – leeward vortices and wake zone.



672  
 673  
 674  
 675  
 676  
 677

**Figure 3.** Vertical profiles of wind components at  $y/H=0$ . The results from SAM are shown by the lines for different number of iterations, from 0 to 3, as indicated in the top-right panel legend. Circles present the CEDVAL data; black and red colors represent the horizontal (u) and vertical (w) wind components, respectively.



678

679

680

681

682

683

684

**Figure 4.** Horizontal profiles of wind components at  $z/H=0.28$ . The results from SAM are shown by the lines for different number of iterations, from 0 to 3, as indicated in the top-right panel legend. Circles present the CEDVAL data; black and red colors represent the horizontal wind components of (u) and (w) wind components, respectively.

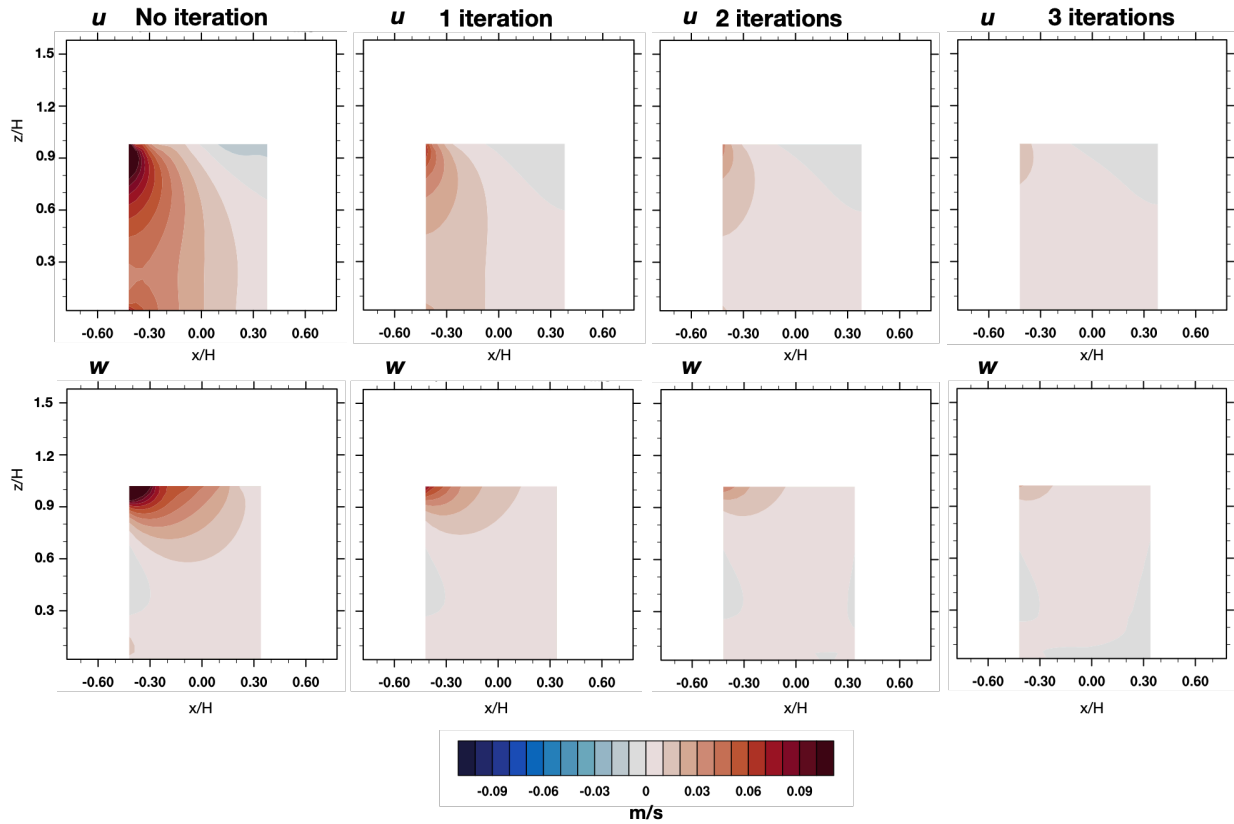


**Figure 5.** Residual horizontal  $u$  (top) and vertical  $w$  (bottom) velocities inside the building at  $y/H=0$  for no additional iteration (left), and several additional iterations over the steps (5)-(8) of the QSBM as indicated above the columns.

685  
686  
687  
688  
689  
690

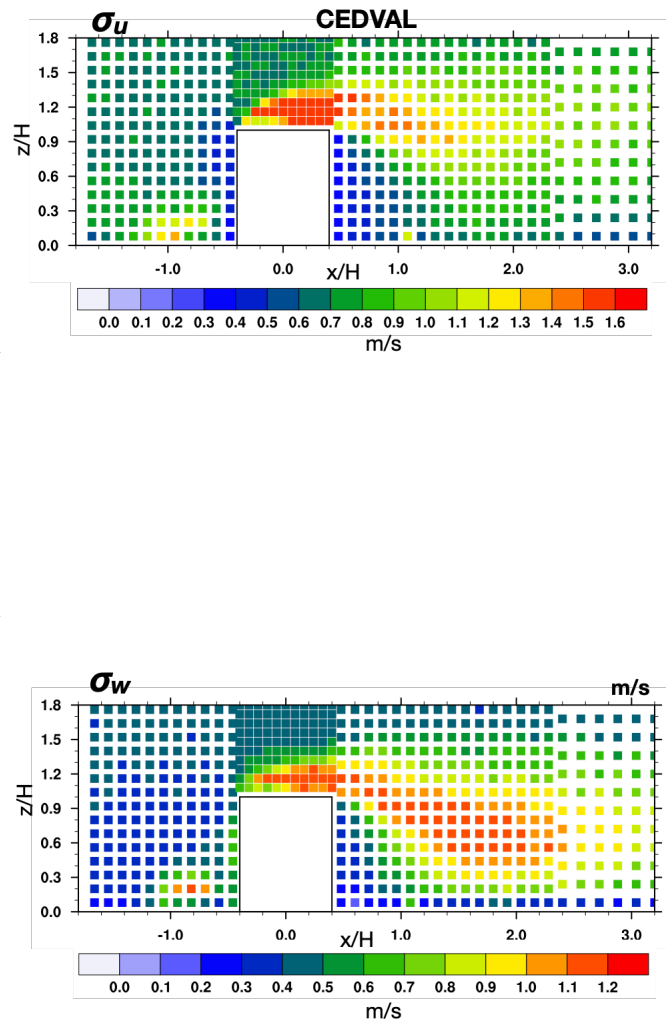
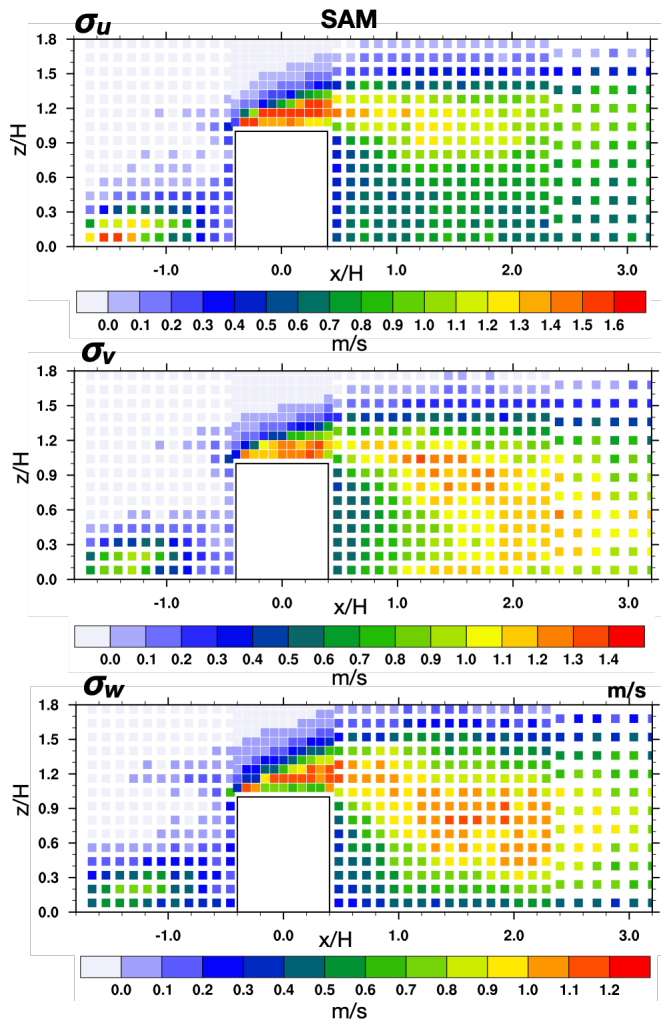


**Figure 6.** Turbulent intensity for different wind components at  $y/H=0$  for SAM (left panels) and CEDVAL observations (right panels). No observations are available for  $v$  component. The measurement density is indicated by the discrete points plotted (i.e., no interpolation is used).

691  
692

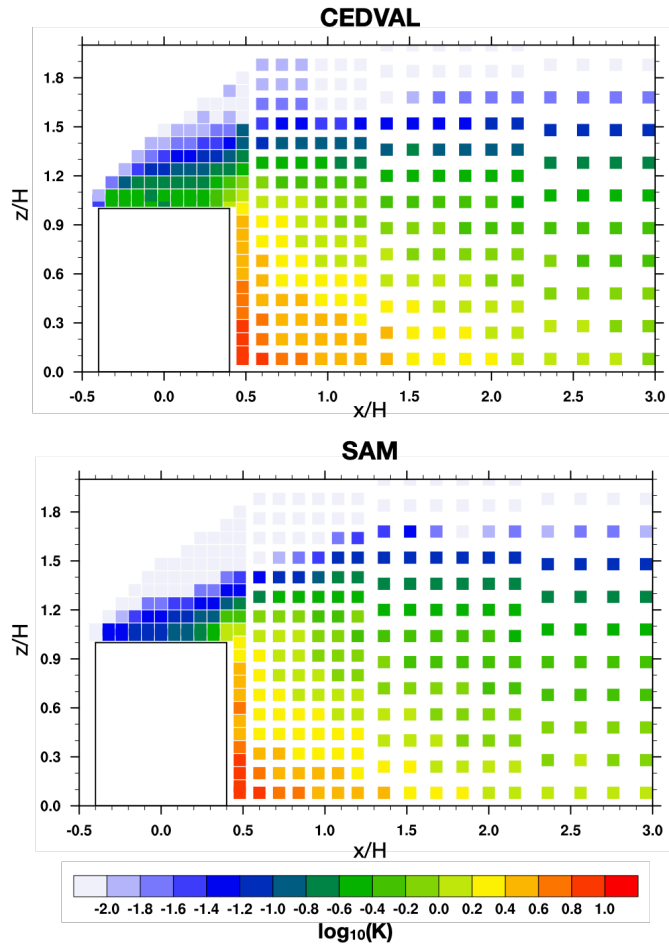


**Figure 7.** The dimensionless gas tracer concentration in the vertical symmetry plane  $y/H=0$  for CEDVAL A1-5 observations (top) and SAM (bottom). The measurement density is indicated by the discrete points plotted (i.e., no interpolation is used).

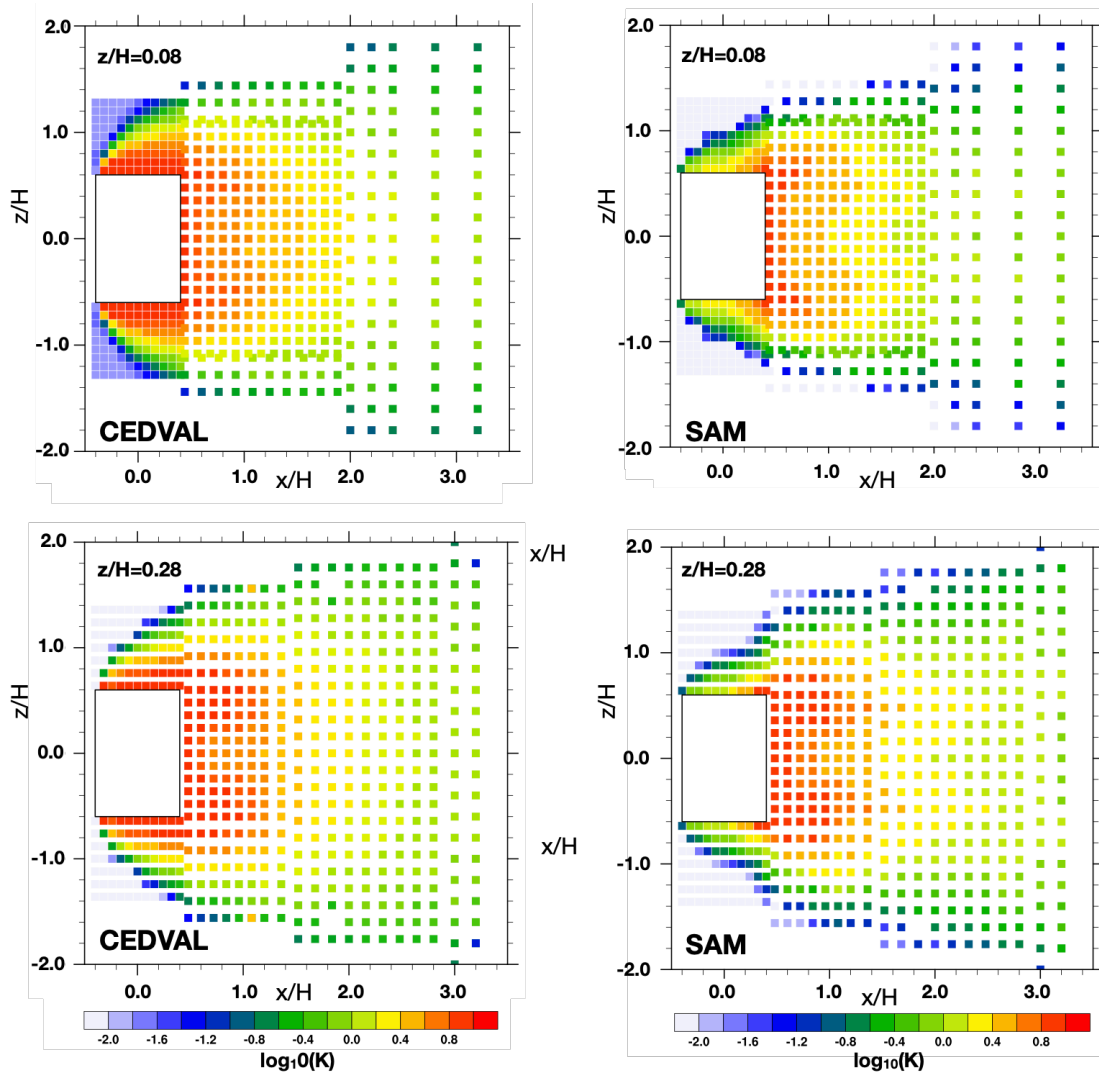


**Figure 8.** The dimensionless gas tracer concentration in the horizontal planes  $z/H=0.08$  (top) and  $z/H=0.28$  (bottom) for CEDVAL A1-5 observations (left) and SAM (right). The measurement density is indicated by the discrete points plotted (i.e., no interpolation is used).

694  
 695  
 696  
 697  
 698  
 699  
 700  
 701  
 702  
 703  
 704

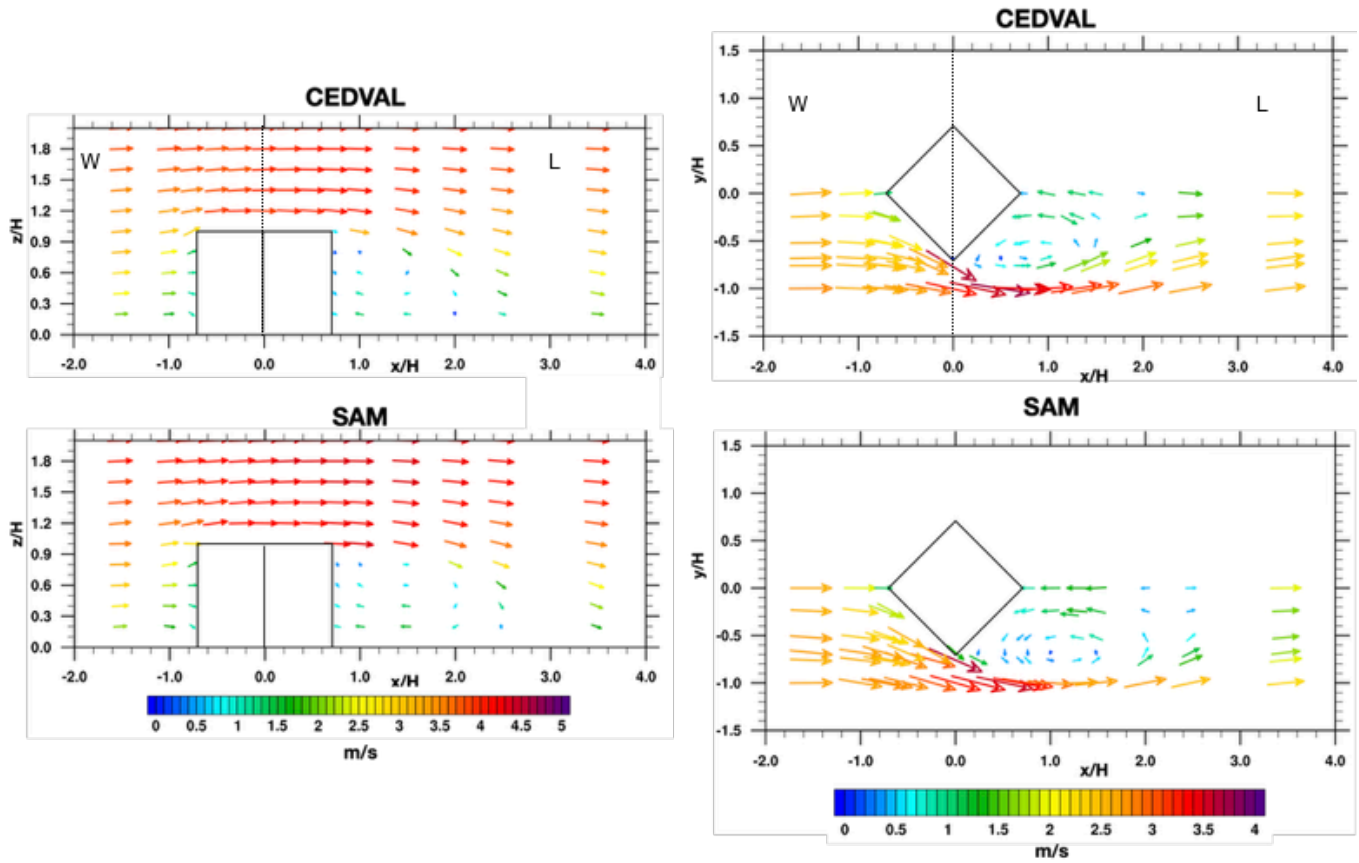


**Figure 9.** Vertical  $x$ - $z$  cross-section at  $y/H = 0$  (left panels) and horizontal  $x$ - $y$  cross-section of wind at  $z/H = 0.4$  (right panels) for CEDVAL A1-6 experiment (top) and SAM simulation (bottom). The coordinates are normalized by the building's height  $H$ . The dashed lines in the top plot indicate the boundaries of the key zones used for statistical comparison: W – windward in front of the building; L – leeward vortex and wake zone.

705  
706  
707  
708  
709  
710  
711  
712  
713  
714  
715  
716  
717

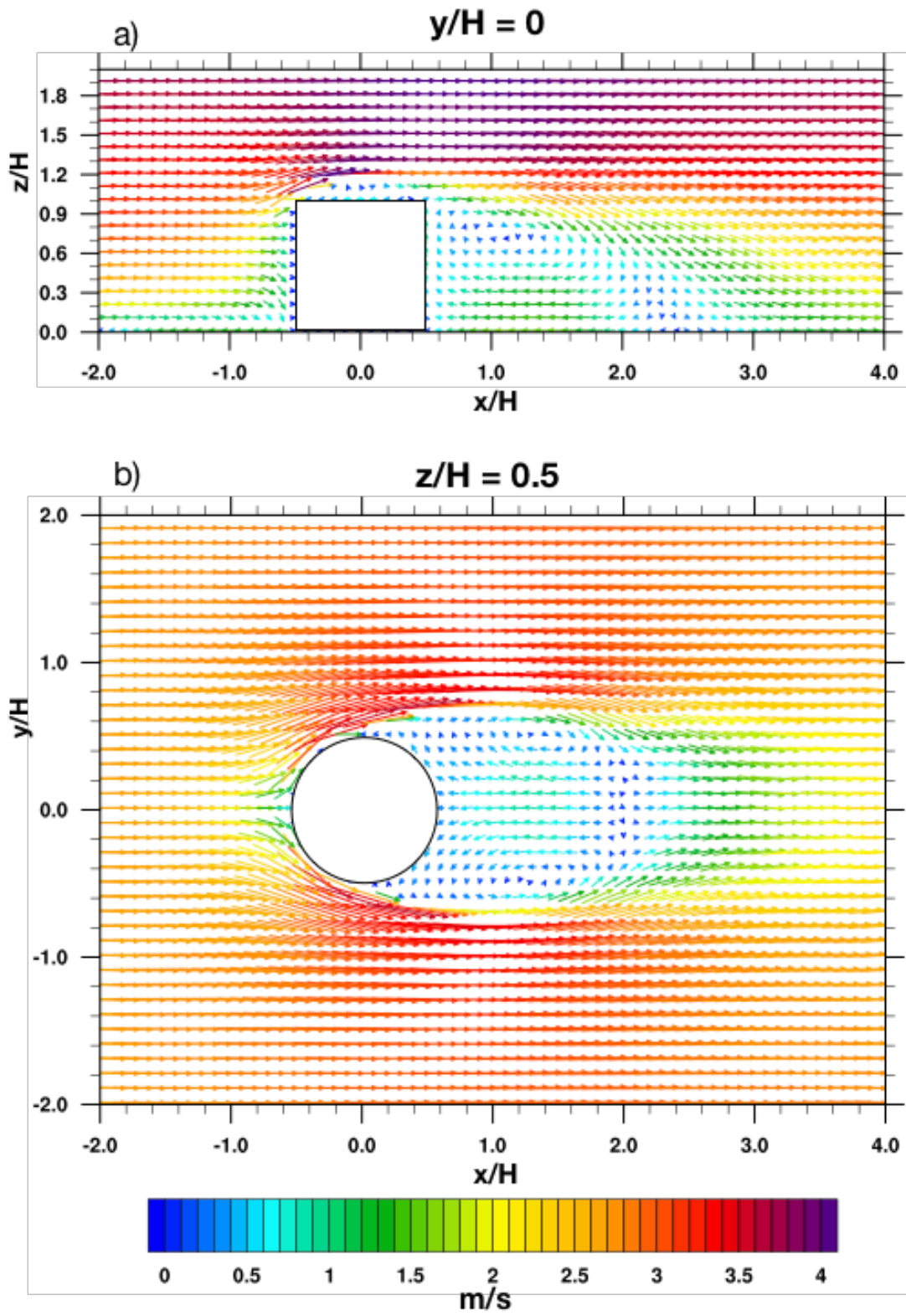
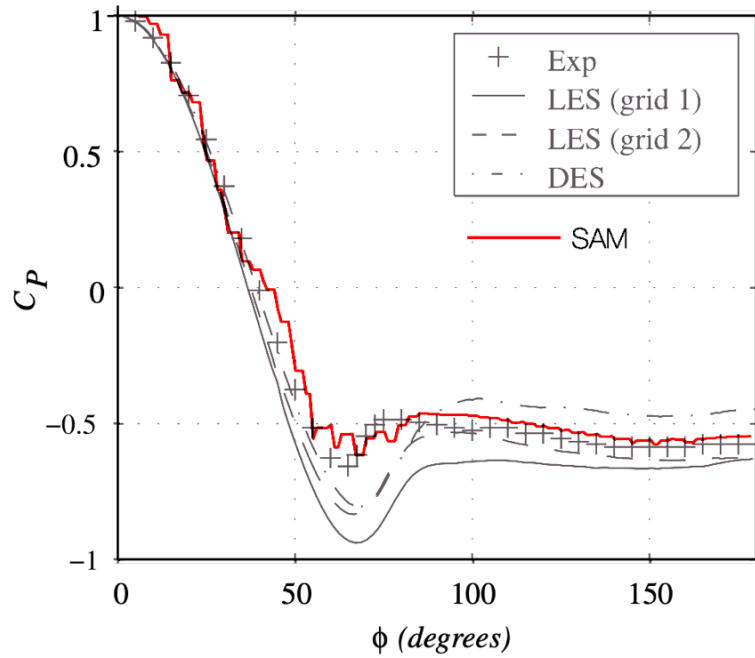


**Figure 10.** (a) Vertical cross-section at  $y/H=0$  and (b) horizontal cross-section at  $z/H=0.5$  of time-averaged wind for simulated flow around a cylinder with aspect ratio of one. The coordinates are normalized by height of the cylinder. The wind magnitude is shown by vector length as well as by its color.

721  
722  
723  
724  
725  
726  
727  
728  
729  
730



731  
732

**Figure 11.** Pressure coefficient  $C_P$  near the surface of the cylinder as a function of cutting angle around it at  $z/H=0.5$ . Results from SAM (red line) are superimposed on Fig. 7 from Pattenden et al (2007), which shows their modeling (LES, DES) and experimental results (Exp).